Observatório Nacional

MASTERS DISSERTATION

ANALYSIS OF THE STATISTICAL ISOTROPY IN THE DISTRIBUTION OF STRUCTURES IN THE LOCAL UNIVERSE

CAMILA NASCIMENTO FRANCO

RIO DE JANEIRO
2023

Ministério da Ciência, Tecnologia, Inovações e Comunicações
Observatório Nacional
Programa de Pós-Graduação

Masters Dissertation

ANALYSIS OF THE STATISTICAL ISOTROPY IN THE DISTRIBUTION OF STRUCTURES IN THE LOCAL UNIVERSE

by

Camila Nascimento Franco

Dissertation submitted to the Faculty of the Graduate Program in Astronomy at the Observatório Nacional, as part of the necessary requirements for the Degree of Master in Astronomy.

Advisor: Dr. Armando Bartolome Bernui Leo

Co-advisor: Dr. Felipe da Silva Ávila

Rio de Janeiro, RJ – Brazil
August 2023

F825 Franco, Camila Nascimento
Análise da isotropia estatística na distribuição de estruturas no Universo Local [Rio de Janeiro] 2023.
xviii, 63 p. 29,7 cm: graf. il. tab.

Dissertação (mestrado) - Observatório Nacional - Rio de Janeiro, 2023.

1. Isotropy. 2. Cosmological Principle. 3. Local Universe. 4. Local Cosmic Void. I. Observatório Nacional. II. Título.

CDU 000.000.000

"ANALYSIS OF THE STATISTICAL ISOTROPY IN THE DISTRIBUTION OF STRUCTURES IN THE LOCAL UNIVERSE"

CAMILA NASCIMENTO FRANCO

DISSERTATION SUBMITTED TO THE FACULTY OF THE GRADUATE PROGRAM IN ASTRONOMY AT THE OBSERVATÓRIO NACIONAL AS PART OF THE NECESSARY REQUIREMENTS FOR A MASTER DEGREE IN ASTRONOMY.

Approved by:

Dr. Armando Bartolome Bernui Leo – ON
(Advisor)

Dr. Felipe da Silva Ávila – ON
(Co-advisor)

Dra. Marina Trevisan – UFRGS

Dr. Ricardo Lourenço Correia Ogando – ON

RIO DE JANEIRO, RJ – BRAZIL
AUGUST 7, 2023

Acknowledgments

To my advisors, Armando Bernui and Felipe Avila, for their generosity in sharing their knowledge of cosmology with me, for their encouragement to keep learning more, for their patience when things didn't go well, and, of course, for their weekly attempts to convince me to like açaí.

To my parents, João and Eliana, who have always supported me in my projects and have done everything to help me achieve my dreams; for their dedication, for always being there, for inspiring me to always do my best. I am very proud to be your daughter.

To my partner and great friend, Sousa Neto, for his companionship, support in difficult times, conversations, laughter, and for taking care of me when I was already at my limit (physically and/or emotionally), for inspiring me every day with his love for knowledge.

To the friends I made along the way, Ayslana Sonally and Bruno Ribeiro, and the 'co-habitants' of Casa Branca, especially Dinorah Teixeira, Ellen Costa-Almeida, Thaís Lemos, and Xyaoyun Shao, for the silliness at lunchtime, an essential moment for all of us. And I couldn't forget the colleagues from the research group, Maria Eduarda Lopes and Fernanda de Oliveira.

To the faculty of ON for the valuable classes and seminars. Particularly, to Dr. Eduardo Telles, Dr. Fernando Roig, Dr. Julio Camargo, Dr. Nacizo Holanda, Dr. Roderik Overzier, with whom I was able to learn more about astronomy through their courses.

To Christianne Garnier and all the staff who provide us with the necessary support to carry out our activities.

To CNPq, for the financial support provided.

Camila Nascimento Franco

ANALYSIS OF THE STATISTICAL ISOTROPY IN THE DISTRIBUTION OF STRUCTURES IN THE LOCAL UNIVERSE

ABSTRACT

We investigate the statistical isotropy of the Local Universe by employing model-independent analyses using the Arecibo Legacy FAST Alfa Survey (ALFALFA) data, which covers a redshift range of $0 < z < 0.06$.

The flat-ΛCDM model currently exhibits the best agreement with observational data obtained from various cosmic tracers. This model is based on the Cosmological Principle, which assumes statistical homogeneity (invariance under translation) and isotropy (invariance under rotation) on large scales.

Our analysis specifically examines the issue of isotropy by exploring the directional characteristics of the Local Universe through the ALFALFA catalog. This catalog encompasses ~ 7000 deg^2 of the sky and includes 31502 extragalactic HI sources divided between the northern and southern Galactic hemispheres. While numerous isotropy analyses have been conducted using cosmic microwave background radiation (CMB) data at $z \simeq 1100$, only a few studies have employed galaxy catalogs, particularly at low redshifts ($z < 0.06$).

Our preliminary findings suggest that the Local Universe is statistically isotropic. However, our analysis reveals the presence of significant underdensities in certain regions, particularly in proximity to the Local Cosmic Void, which was initially described by Tully & Fisher (1987). To assess isotropy, we utilized the two-point angular correlation function, employing the Landy-Szalay estimator as statistical measure. Additionally, we employed log-normal simulations (which consider the best Planck's cosmological parameters) to estimate uncertainties.

To gain insight into the properties and morphology of the examined structure, we determined the parameters θ_0 (the transition scale between nonlinear and linear regimes) and β (which quantifies matter clustering) at small and large scales. Furthermore, we evaluated the statistical significance of our results, conducted complementary tests using simulated voids, and performed comparative investigations by referring to existing literature on voids in the Local Universe. Our findings indicate that, apart from the Local Cosmic Void (with a number-density contrast of $\delta \simeq -0.7$), the region covered by the ALFALFA survey also encompasses partially other underdense regions or voids, including the Dipole Repeller.

List of Figures

1.1 Local Cosmic Void 2

2.1 Possible cases of three-space curvature 7
2.2 Evolution of the energy densities 9
2.3 Hubble diagram 11
2.4 Comoving Distance 15
2.5 Angular Diameter Distance 16
2.6 CMB spectrum 18

3.1 Histogram of the redshift distribution of the ALFALFA data 22
3.2 Footprint of the ALFALFA catalog in equatorial coordinates 23
3.3 Footprint of the ALFALFA division in 10 sky patches 24
3.4 Comparison between the observational data and its respective random catalog 26
3.5 Example of a log-normal mock catalog 28
3.6 Comparison between the observational data and its respective mock catalog 29

4.1 Correlation matrix for 100 log-normal mocks 35

5.1 Mosaic of the 2PACF for large-angle analysis 38
5.2 Distribution of the best-fit parameter β^S from small-angle analyses of 1000 Area-mocks 39
5.3 Distance distribution histogram of the ALFALFA sample 42
5.4 Analysis of the Areas 2, 9 and 10 with the Cumulative Distribution Function 43
5.5 Toy-model simulation 44
5.6 Toy-model experiment, simulating a void region with $\delta = -0.7$ 44
5.7 2PACF analyses for a toy-model simulation 45
5.8 ALFALFA footprint in Galactic coordinates 46
5.9 Null test for the random data set 47
5.10 Mosaic of the 2PACF for small-angle analysis 48

A.1 Toy-model experiment of the cumulative distribution function 63

List of Tables

3.1 Properties of the ten analyzed regions 24
3.2 Survey configuration used to generate a set of 1000 log-normal mock catalogs 27
3.3 Cosmological parameters 27

5.1 Best-fit parameters considering the power-law relationship 40

List of Symbols

A_s	Primordial comoving curvature power spectrum amplitude, p. 27
G	Newton's universal gravitational constant, p. 5
H_0	Hubble constant, p. 11
N_g	Número de galáxias, p. 27
R	Ricci scalar, p. 5
R_0	Physical curvature today, p. 6
$R_{\mu\nu}$	Ricci tensor, p. 5
$T_{\mu\nu}$	Stress-energy tensor, p. 5
$\Omega_b h^2$	Baryon density, p. 27
$\Omega_c h^2$	Cold dark matter density, p. 27
Σm_ν	Sum of the masses of neutrinos, p. 28
α	Right ascension, p. 23
β	Clustering of matter parameter, p. 33
δ	Declination, p. 23
$\omega(\theta)$	Two-Point Angular Correlation Function, p. 32
$\rho(t)$	Density of the cosmic fluid, p. 7
θ_0	Transition parameter between the linear and non-linear regimes, p. 33
$\xi(r)$	Two-point Correlation Function, p. 31
$a(t)$	Scale factor, p. 6
b	Bias, p. 27

c	Speed of light, p. 5
d_A	Angular diameter distance, p. 16
d_L	Luminosity distance, p. 15
d_p	Proper distance, p. 13
$g_{\mu\nu}$	Components of the metric tensor, p. 5
h	Dimensionless Hubble constant, p. 28
k	Normalized curvature constant, p. 6
n	Number density, p. 21, 24
n_s	Scalar spectral index, p. 28
$p(t)$	Pressure of the fluid, p. 7
t	Cosmic time, p. 6
z	Cosmological redshift, p. 13
HI	Neutral Hydrogen, p. 3
h	Dimensionless Hubble constant, p. 11
n	Number density, p. 31

List of Abbreviations

ΛCDM	Λ Cold Dark Matter, p. 1, 3, 5, 8
2PACF	Two-Point Angular Correlation Function, p. 3, 31
2PCF	Two-point correlation function, p. 31
ALFALFA	Arecibo Legacy Fast ALFA Survey, p. 3, 21, 23, 27
BAO	Baryon Acoustic Oscillations, p. 1
CDM	Cold Dark Matter, p. 17
CMB	Cosmic Microwave Background, p. 1, 17, 18
COBE	COsmic Background Explorer, p. 18
CP	Cosmological Principle, p. 1
DEC	Declination, p. 31
FIRAS	Far InfraRed Absolute Spectrophotometer, p. 18
FLRW	Friedmann-Lemaître-Robertson-Walker, p. 5, 6, 13
HDM	Hot Dark Matter, p. 17
LCV	Local Cosmic Void, p. 2, 3
LS	Landy-Szalay estimator, p. 32
LU	Local Universe, p. 1
NGH	Northern Galactic Hemisphere, p. 21, 23, 24
OC	Optical Counterpart, p. 23
PH	Peebles-Hauser estimator, p. 32
RA	Right Ascension, p. 31
SGH	Southern Galactic Hemisphere, p. 23, 24

SNR	Signal-to-noise ratio, p. 23
WMAP	Wilkinson Microwave Anisotropy Probe, p. 18

Contents

List of Figures ix

List of Tables xi

List of Symbols xiii

List of Abbreviations xv

1 Introduction 1

2 Fundamentals of Modern Cosmology 5

2.1 Friedmann-Lemaître-Robertson-Walker (FLRW) metric . . . 5

2.2 Spacetime dynamics . . . 6

2.2.1 Friedmann equations . . . 7

2.2.2 Background Cosmological parameters . . . 9

2.3 Expansion . . . 10

2.3.1 Hubble-Lemaître Law . . . 10

2.3.2 Cosmological redshift . . . 12

2.4 Cosmological distances . . . 13

2.4.1 Proper Distance . . . 13

2.4.2 Comoving Distance . . . 14

2.4.3 Luminosity Distance . . . 15

2.4.4 Angular Diameter Distance . . . 16

2.5 Cosmological Observables . . . 16

2.5.1 Accelerated expansion . . . 17

2.5.2 Dark matter . . . 17

2.5.3 Cosmic Microwave Background Radiation (CMB) . . . 17

3 Data selection and synthetic catalogs 21

3.1 Observational data: the ALFALFA catalog . . . 21

3.1.1 General characteristics . . . 21

3.1.2 Selection criteria . . . 23

3.2 Synthetic catalogs . . . 24

3.2.1 Random catalogs . . . 25
3.2.2 Log-normal mocks catalogs . . . 25

4 Statistical methods **31**
4.1 Two-Point Angular Correlation Function (2PACF) . . . 31
4.2 Estimation of uncertainties . . . 34

5 Results and discussions **37**
5.1 Statistical isotropy analyses with the 2PACF . . . 37
5.2 Sky patches with intriguing features . . . 40
5.2.1 Cumulative Distribution Function . . . 41
5.3 LS versus PH . . . 43
5.4 Robustness, consistency, and null tests . . . 45

6 Conclusions **49**

Bibliography **51**

A Toy-model simulation of the cumulative distribution function **63**

Chapter 1

Introduction

One of the pillars of the ΛCDM (Λ is the cosmological constant and CDM means *Cold Dark Matter*) model, the Cosmological Principle (CP) is based on the assumption of statistical homogeneity and statistical isotropy, meaning that on large scales –around 100 Mpc (COLEMAN and PIETRONERO, 1992; HOGG *et al.*, 2005; LAURENT *et al.*, 2016; NADATHUR, 2013; SARKAR *et al.*, 2009; SARKAR and PANDEY, 2016; SCRIMGEOUR *et al.*, 2012) and, in the Local Universe, 20° (AVILA *et al.*, 2019)–, the universe is statistically homogeneous and isotropic. Homogeneity refers to translation invariance (inexistence of privileged locations), while isotropy refers to rotational invariance (absence of privileged directions) (RYDEN, 2003; SCHUTZ, 2009). Although they usually go hand in hand, homogeneity and isotropy are independent. This means that one does not necessarily imply the other. In other words, we can have homogeneity without isotropy (and vice versa). However, a theorem establish that isotropy across all points directly implies homogeneity (SCHUTZ, 2009).

Another important point is that, as we consider smaller scales, we observe that the universe becomes increasingly clumpy. The presence of structures such as planets, clusters, and voids becomes more relevant, and the clustering of structures becomes more evident. Therefore, in analyses of the CP we must take into account the statistical aspect of homogeneity and isotropy.

The CP has been tested using data from various astronomical surveys with different tracers (ALURI *et al.*, 2022; APPLEBY and SHAFIELOO, 2014; AVILA *et al.*, 2019, 2022; BENGALY *et al.*, 2019, 2018; BOLEJKO and WYITHE, 2009; SYLOS LABINI and BARYSHEV, 2010), such as quasars (FUJII, 2022; GONÇALVES *et al.*, 2018a, 2021; SECREST *et al.*, 2021), CMB (BERNUI, 2008; HANSEN *et al.*, 2004; KHAN and SAHA, 2022; MARQUES *et al.*, 2018), gravitational waves (GALLONI *et al.*, 2022), short gamma-ray bursts (BERNUI *et al.*, 2008), BAO (GONÇALVES *et al.*, 2018b), and galaxies (BENGALY *et al.*, 2017).

Furthermore, it is of interest to apply the CP to the Local Universe (LU), due to our lack of knowledge of all the structures present and how they are clustered, in particular

because many of these structures are hidden to us by the Milky Way disc (GUAINAZZI *et al.*, 2005; HWANG and GELLER, 2013). An example of a structure that is still surrounded by many questions is the Local Cosmic Void (LCV), which is located in the vicinity ($\sim$ 1 Mpc) of the Local Group (HOFFMAN *et al.*, 2017; TULLY *et al.*, 2019; WHITBOURN and SHANKS, 2014), as illustrated in Figure 1.1.

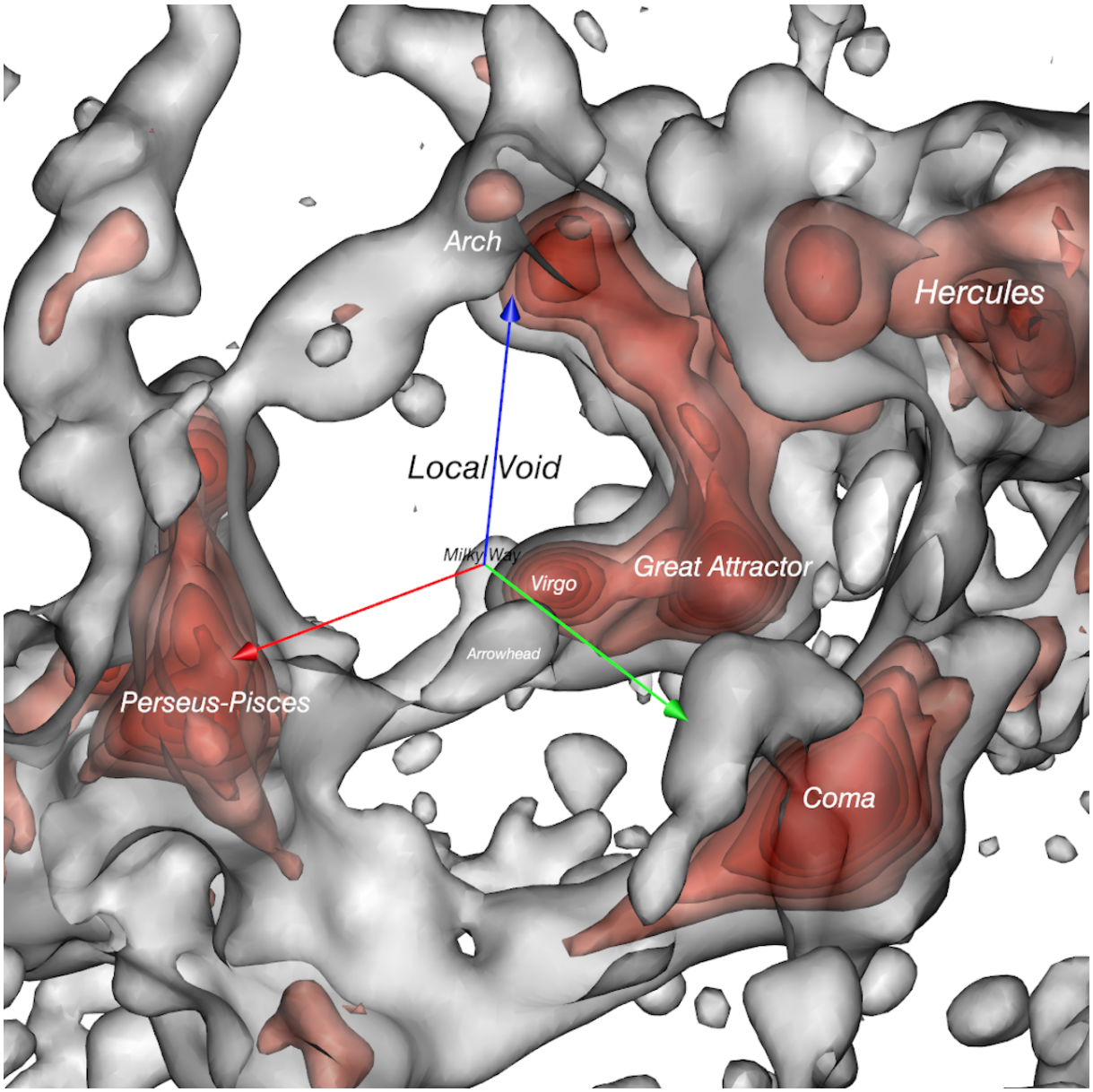

Figure 1.1: Overview of the structure surronding the Local Cosmic Void. The LCV fills the empty region above the Milky Way, which is at the origin of the colored arrows (TULLY *et al.*, 2019).

First described by TULLY and FISHER (1987), this structure has a low density of luminous matter inside, but we still do not have all the information about its main features: location, size, shape, etc. Recent studies suggest that the LCV is a $150 - 300$ Mpc void (BÖHRINGER *et al.*, 2020; PLIONIS and BASILAKOS, 2002; TULLY *et al.*, 2008,

2013, 2019; WHITBOURN and SHANKS, 2014, 2016), and it is these dimensions that make it relevant (KEENAN *et al.*, 2013; TULLY *et al.*, 2019). Another interesting characteristic is the dynamical effects caused by it, such as high peculiar velocities in nearby galaxies (moving away from the LCV at a velocity of $260\,\mathrm{km\ s^{-1}}$) (HOFFMAN *et al.*, 2017; TULLY *et al.*, 2008, 2013, 2019); this information is important, for instance, for calibrating standard candles that help measure H_0.

The presence of filaments, with clusters at their intersections, and voids is predicted by the ΛCDM model (PANDEY *et al.*, 2011; PEEBLES, 2001; SARKAR *et al.*, 2022; SPRINGEL *et al.*, 2006; VOGELSBERGER *et al.*, 2014). However, a void with the dimensions of the LCV can pose a challenge for the current model (PEEBLES and NUSSER, 2010), unless its apparent huge size is caused by an observational effect and these structures are actually a collection of interconnected smaller voids (FRANCO *et al.*, 2023; MOORMAN *et al.*, 2014).

Thus, in addition to dedicating ourselves to the study of the properties of statistical isotropy in the Local Universe, we also investigated how void structures are distributed in our sample. For this purpose, we chose the ALFALFA catalog (Arecibo Legacy Fast ALFA Survey), which detected extragalactic sources of HI clouds at 21 cm in the redshift range $z < 0.06$, and divided it into a reasonable number of patches. We used the two-point angular correlation function (2PACF) –which only requires data projected onto the celestial sphere (right ascension and declination)– as our statistical gauge, thus that our analyses were independent (or weakly dependent) on cosmological model hypotheses.

This dissertation is structured as follows: in Chapter 2, the foundations of modern cosmology will be presented, which are relevant for understanding the definitions used throughout the work. Then, the data selection criteria will be detailed in Chapter 3, as well as the process of producing synthetic catalogs used to estimate the 2PACF and the uncertainties associated with the measurements. The statistical methods used to examine the final sample will be addressed in Chapter 4, and our results will be presented and discussed in Chapter 5. Finally, our conclusions will be summarized in Chapter 6.

Chapter 2

Fundamentals of Modern Cosmology

In this chapter, the theoretical foundations of the ΛCDM cosmological model and relevant topics for the study of cosmology will be introduced. In Section 2.1, the Friedmann-Lemaître-Robertson-Walker (FLRW) metric will be presented, providing the necessary knowledge to understand the dynamics of spacetime in terms of the Friedmann equations (Section 2.2). In Section 2.3, the Hubble-Lemaître Law and the cosmological redshift will be briefly introduced. Then, in Section 2.4, the determination of cosmological distances will be addressed. Finally, in Section 2.5, the main observational foundations of cosmology will be summarized.

2.1 Friedmann-Lemaître-Robertson-Walker (FLRW) metric

The dynamics of the universe in the context of General Relativity can be understood through the interaction between the geometry of spacetime and the energetic content it contains (EINSTEIN, 1905). The interaction between the geometry and the matter-energy content is mathematically described by the equations developed by Einstein, written as

$$R_{\mu\nu} - \frac{1}{2} g_{\mu\nu} R = \frac{8\pi G}{c^4} T_{\mu\nu}, \tag{2.1}$$

where $R_{\mu\nu}$ is the Ricci tensor, $g_{\mu\nu}$ are the components of the metric tensor, R is the Ricci scalar, $T_{\mu\nu}$ is the stress-energy tensor, G is the Newton's universal gravitational constant and c is the speed of light (ROOS, 2015).

When weak gravitational fields and non-relativistic velocities, $v \ll c$, are considered, the Einstein equations (2.1) reduce to the Newtonian limit, given by the Poisson equation for Newtonian gravity in the presence of a density $\rho(x,\, y,\, z)$, in the form

$$\vec{\nabla}^2 \Phi(x,\, y,\, z) \simeq 4\pi G \rho(x,\, y,\, z). \tag{2.2}$$

The solution of the Einstein equations requires the definition of a metric $g_{\mu\nu}$ and an energy-momentum tensor $T_{\mu\nu}$. The content of a locally homogeneous and isotropic spacetime is represented by a fluid with pressure p, a four-velocity vector $u^\mu = dx^\mu/d\tau$ (where τ is the proper time), and a density ρ, according to

$$T_{\mu\nu} = (\rho + p/c^2)u^\mu u^\nu + p g_{\mu\nu}. \tag{2.3}$$

When we assume homogeneity and isotropy, locally, the intrinsic curvature is constant, and we use the FLRW (Friedmann-Lemaître-Robertson-Walker) metric (BAUMANN, 2022; PETTINI, 2018),

$$ds^2 = -c^2dt^2 + a^2(t)\left[\frac{dr^2}{1-k\frac{r^2}{R_0^2}} + r^2(d\theta^2 + \sin^2\theta d\phi^2)\right], \tag{2.4}$$

where t is the cosmic time, $a(t)$ is the scale factor that measures the rate of expansion of spacetime, k is the normalized curvature constant, and R_0 is the physical curvature today (BAUMANN, 2022).

Conveniently, one adopts a change of variable for the radial coordinate r by making the substitution:

$$d\chi \equiv \frac{dr}{\left(1-k\frac{r^2}{R_0^2}\right)^{1/2}}, \tag{2.5}$$

which results in

$$ds^2 = -c^2dt^2 + a^2(t)[d\chi^2 + S_k^2(\chi)(d\theta^2 + \sin^2\theta d\phi^2)], \tag{2.6}$$

where

$$S_k(\chi) \equiv \begin{cases} R_0 \sinh\left(\frac{\chi}{R_0}\right) & \text{for } k = -1, \\ \chi & \text{for } k = 0, \\ R_0 \sin\left(\frac{\chi}{R_0}\right) & \text{for } k = +1. \end{cases} \tag{2.7}$$

The normalized curvature constant takes the values $k = 0$ when space is flat, $k = -1$ when there is negative curvature (hyperbolic space), or $k = +1$ when there is positive curvature (spherical space). The three cases are illustrated in Figure 2.1 for the bidimensional case.

2.2 Spacetime dynamics

In this section, we will explore the Friedmann equations (Subsection 2.2.1), which describe the expansion of the universe and are of great importance for cosmology. We will then introduce the background cosmological parameters (Subsection 2.2.2), dimensionless quantities that are observationally measured and are related to the Friedmann equations.

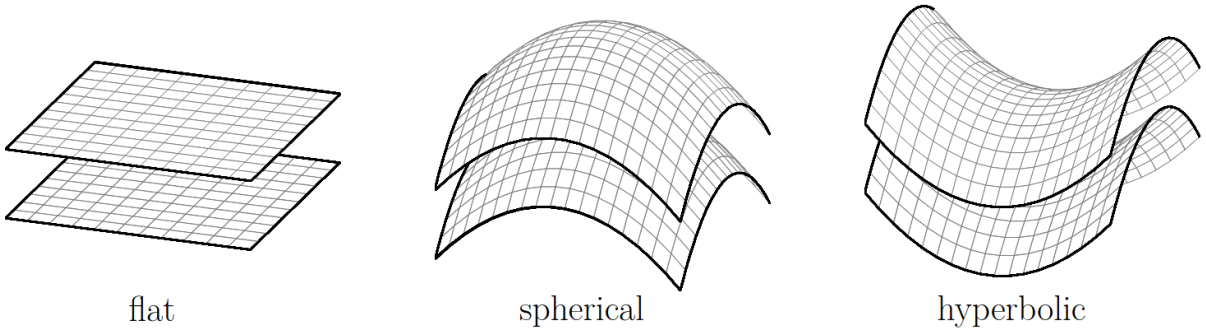

Figure 2.1: The three-space can be flat, spherical or hyperbolic. The first one is the simplest possibility. The next one is the spherical case, which has constant positive curvature. The last one is the hyperbolic possibility, with constant negative curvature. In this figure, we illustrate these three geometries for the two-dimensional case (BAUMANN, 2022).

2.2.1 Friedmann equations

Starting from Equations (2.4) and (2.1), assuming a perfect fluid with no viscosity, no heat conduction (adiabatic), described by Equation (2.3), and considering the assumptions of homogeneity and isotropy, we arrive at two independent solutions, collectively called the *Friedmann equations* (BAUMANN, 2022; SCHUTZ, 2009). The first equation describes the evolution of the scale factor[1] of the universe, denoted by $a(t)$, and is given by

$$\left[\frac{\dot{a}(t)}{a(t)}\right]^2 = \frac{8\pi G}{3}\rho(t) - \frac{kc^2}{a^2(t)R_0^2}, \tag{2.8}$$

where $\cdot$ represents the derivative with respect to cosmic time, $\rho(t)$ is the density, and $p(t)$ is the pressure of the fluid (RYDEN, 2003; SCHUTZ, 2009). The second equation provides information about the acceleration of the spacetime and is given by

$$\frac{\ddot{a}(t)}{a(t)} = -\frac{4\pi G}{3}\left[\rho(t) + \frac{3p(t)}{c^2}\right]. \tag{2.9}$$

For the usual kind of matter, $[\rho(t) + 3p(t)/c^2] > 0$ implying that $\ddot{a} < 0$, which means that the expansion is gradually slowing down over time until it stops (PADMANABHAN, 1993).

Additionally, there is a third equation obtained by taking the time derivative of Equation (2.8),

$$\frac{\dot{a}\ddot{a}}{a^2} - \frac{\dot{a}^3}{a^3} - \frac{kc^2}{R_0^2}\frac{\dot{a}}{a^3} = \frac{4\pi G}{3}\dot{\rho}, \tag{2.10}$$

[1] The scale factor is a dimensionless quantity.

substituting Equation (2.9) into Equation (2.10),

$$\frac{\dot{a}}{a}\left[-\frac{4\pi G}{3}\left(\rho+\frac{3p}{c^2}\right)\right]-\frac{\dot{a}^3}{a^3}-\frac{kc^2}{R_0^2}\frac{\dot{a}}{a^3}=\frac{4\pi G}{3}\dot{\rho}. \tag{2.11}$$

Finally, using Equation (2.8), we found that

$$\dot{\rho}+3\frac{\dot{a}}{a}\left(\rho+\frac{p}{c^2}\right)=0, \tag{2.12}$$

which expresses the conservation of energy and is known as the *fluid equation* (BAUMANN, 2022).

Thus, we have a system of equations that can be solved by resorting to the linear relationship for the perfect fluids between pressure and density, as prescribed by the equation of state

$$p(t)=w\rho(t)c^2, \tag{2.13}$$

where the parameter w has a specific value for each component present in the universe. The solution to Equation (2.12) will then be obtained through the integration

$$\int_{\rho}^{\rho_0}\frac{d\rho'}{\rho'}=-3(1+\omega)\int_{a}^{a_0}\frac{da'}{a'}, \tag{2.14}$$

which, for a constant ω, results in

$$\rho(a)=\rho_0 a(t)^{-3(1+\omega)}. \tag{2.15}$$

According to the concordance cosmological model, ΛCDM, there are three main components that describe the material content of the universe: matter, radiation, and dark energy. Matter is a non-relativistic component and can be either baryonic (protons, neutrons, and electrons[2]) or dark, with $\omega=0$; radiation has $\omega=1/3$; and dark energy has $\omega=-1$ (PETTINI, 2018; RYDEN, 2003). Substituting these values into Equation (2.15), we get

$$\rho_m(t)=\rho_{m0}a(t)^{-3}, \tag{2.16}$$

$$\rho_r(t)=\rho_{r0}a(t)^{-4}, \tag{2.17}$$

$$\rho_\Lambda=\rho_{\Lambda 0}. \tag{2.18}$$

In each phase the universe went through, one of these components was dominant, as can be observed in Figure 2.2. Initially, radiation was the dominant component until the radiation-matter equality at $a_{rm}\approx 3\times 10^{-4}$ ($t_{rm}\approx 0.05$ Myr). Then, matter became dominant until $a_{m\Lambda}\approx 0.77$ ($t_{m\Lambda}\approx 10$ Gyr). Currently, at $a_0=1$ ($t_0\approx 14$ Gyr), dark

[2]Electrons are charged leptons, but since they have much smaller masses compared to protons, this grouping is accepted (PETTINI, 2018; RYDEN, 2003).

energy is the dominant component of the universe (BAUMANN, 2022; PETTINI, 2018; RYDEN, 2003).

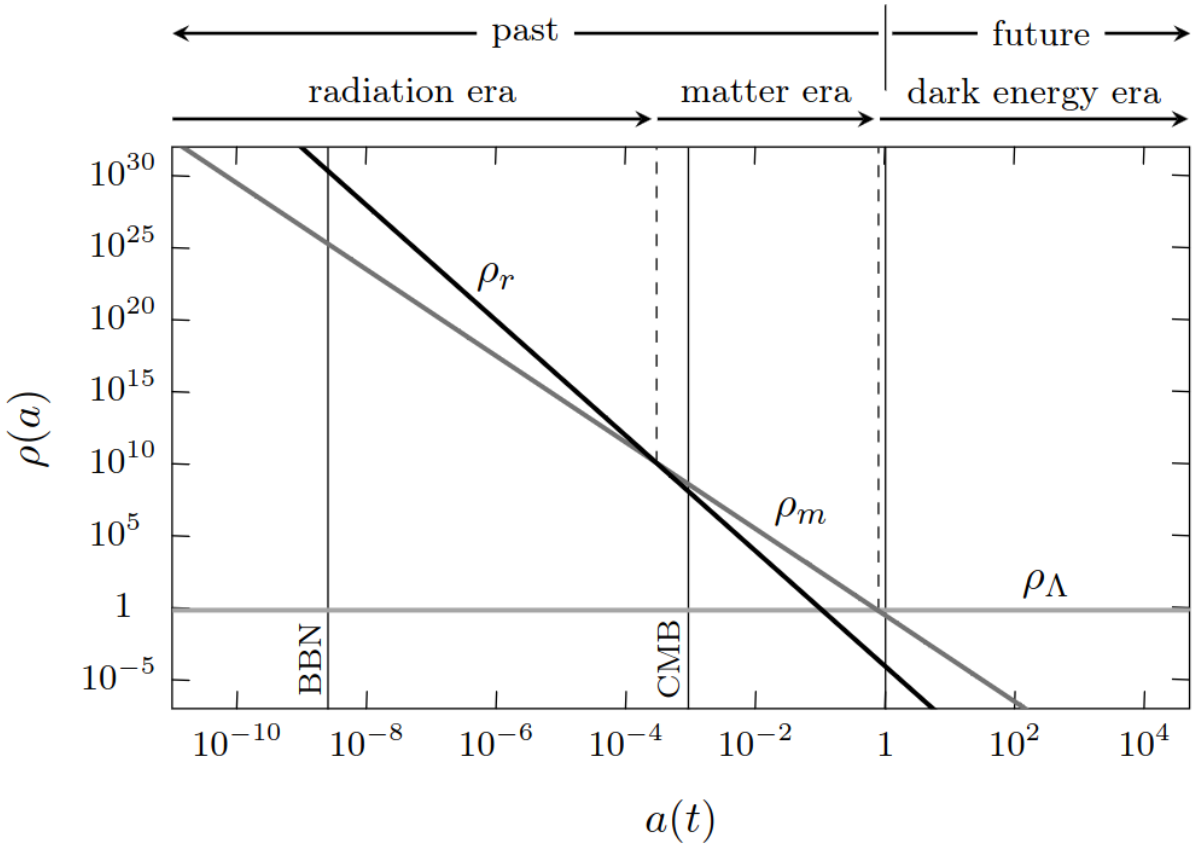

Figure 2.2: The evolution of energy densities is as follows: initially, radiation is the dominant component. Then, matter becomes dominant, and finally, the era of dark energy is reached (BAUMANN, 2022).

2.2.2 Background Cosmological parameters

Taking Equation (2.8) and considering that the curvature is $k = 0$, we find that the value of $\rho(t)$ at which the universe is flat, called the critical density, $\rho_c(t)$, is given by (LIDDLE, 2003).

$$\rho_c(t) = \frac{3H^2(t)}{8\pi G}, \tag{2.19}$$

where the definition of the Hubble parameter, which measures the rate of expansion of the universe at time t, was introduced as

$$H(t) \equiv \frac{\dot{a}(t)}{a(t)}. \tag{2.20}$$

If we have a total energy density greater than ρ_c, the corresponding geometry will be spherical; conversely, for a total density smaller than ρ_c, the geometry will be hyperbolic.

It is useful to compare the density of the universe with the critical value. For this purpose, we define the dimensionless *density parameter*, $\Omega(t)$, as follows

$$\Omega(t) \equiv \frac{\rho(t)}{\rho_c(t)}. \tag{2.21}$$

Consequently, we have the density parameters for matter, radiation, dark energy, and curvature, respectively, given by

$$\Omega_m(t) \equiv \frac{8\pi G\rho_m(t)}{3H^2(t)}, \tag{2.22}$$

$$\Omega_r(t) \equiv \frac{8\pi G\rho_r(t)}{3H^2(t)}, \tag{2.23}$$

$$\Omega_\Lambda(t) \equiv \frac{8\pi G\rho_\Lambda(t)}{3H^2(t)}, \tag{2.24}$$

$$\Omega_k(t) \equiv -\frac{kc^2}{a^2R_0^2H^2(t)} = 1 - \Omega_m - \Omega_r - \Omega_\Lambda. \tag{2.25}$$

By substituting Equations (2.20), (2.22), (2.23), (2.24), and (2.25) into Equation (2.8), and using the results of Equations (2.16), (2.17), and (2.18), the Friedmann equation can be written as

$$\left[\frac{H(t)}{H_0}\right]^2 = \Omega_r a^{-4}(t) + \Omega_m a^{-3}(t) + \Omega_k a^{-2}(t) + \Omega_\Lambda. \tag{2.26}$$

2.3 Expansion

The recession of galaxies is a key element in the evidence that the universe is expanding. Therefore, due to its importance, a brief historical overview of the Hubble-Lemaître law will be presented in Subsection 2.3.1. Following that, the concept of cosmological redshift will be developed to establish its relation with the scale factor.

2.3.1 Hubble-Lemaître Law

In 1929, Edwin Hubble demonstrated that the redshift and distance of galaxies are directly proportional (HUBBLE, 1929), based on the measurements in the Figure 2.3 (for more details on the development of the Hubble diagram, see KIRSHNER (2004)). Moreover, in a collaborative work with Milton Humason, this proportionality was confirmed for even larger distances (HUBBLE and HUMASON, 1931). Even earlier, in 1927, Georges Lemaître had published a similar result in a less circulated journal, written in French, which made his findings unknown for some time (LEMAÎTRE, 1927).

The contributions of Hubble and Lemaître gave rise to the law that now bears both

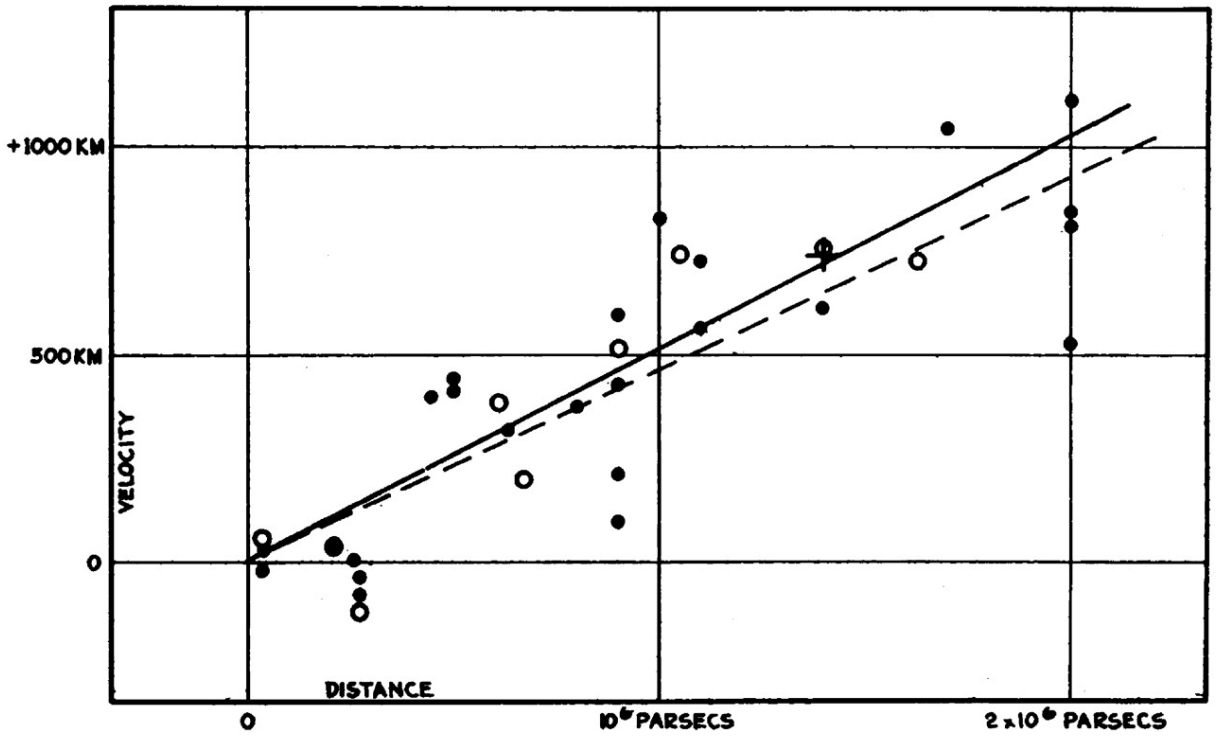

Figure 2.3: The Hubble diagram shows the velocity–distance relation among extragalactic nebulae. Note that the horizontal axis represents distances in units of parsec, and the vertical axis corresponds to velocities cz, However, there is an error in the units, which should be km/s (HUBBLE, 1929).

their names –the Hubble-Lemaître Law– and is written as

$$cz = H_0 d, \tag{2.27}$$

where H_0 is the Hubble constant measured today, $t = t_0$, and can be expressed in terms of the dimensionless Hubble constant, h,

$$h \equiv \frac{H_0}{100 \mathrm{km\,s^{-1}\,Mpc^{-1}}}. \tag{2.28}$$

Currently, according to the measurements by RIESS *et al.* (2016), the value of this constant is[3]

$$H_0 = 73.8 \pm 2.4 \mathrm{km\,s^{-1}\,Mpc^{-1}}. \tag{2.29}$$

The equation (2.27) can be rewritten using the non-relativistic approximation $v = cz$. Thus, we have

$$v = H_0 d, \tag{2.30}$$

where v is the radial velocity of galaxies. This expression is valid only at low redshifts

[3]Notice, however, that there is currently a tension in the measurements of h (DI VALENTINO *et al.*, 2021).

($z \lesssim 0.2$; RYDEN (2003)). Therefore, we conclude that there is a recession of galaxies, indicating an expansion of our universe.

Isotropy states that observers in different positions in space should perceive the same recession of nearby galaxies relative to their own position. Therefore, the Hubble-Lemaître law is a consequence of this assumption in the universe.

2.3.2 Cosmological redshift

When considering the propagation of a photon in the framework of General Relativity, it follows a null geodesic ($ds = 0$). Assuming a radial displacement ($d\theta = d\phi = 0$), Equation (2.4) reduces to

$$\frac{cdt}{a(t)} = \pm \frac{dr}{\left(1 - k\frac{r^2}{R_0^2}\right)^{1/2}}, \tag{2.31}$$

in which the positive sign indicates emission and the negative sign, the reception of a photon.

If two photons are emitted, one at time t_e and the other at time $t_e + \delta t_e$, and received at times t_0 and $t_0 + \delta t_0$[4], respectively, the total time it takes for the first light ray to travel from $r = 0$ to $r = r_0$ is given by the integral (LIDDLE, 2003; THEUNS, 2021)

$$\int_{t_e}^{t_0} \frac{cdt}{a(t)} = \int_0^{r_0} \frac{dr}{\left(1 - k\frac{r^2}{R_0^2}\right)^{1/2}}, \tag{2.32}$$

while the second one will travel the same path with a total time given by

$$\int_{t_e+\delta t_e}^{t_0+\delta t_0} \frac{cdt}{a(t)} = \int_0^{r_0} \frac{dr}{\left(1 - k\frac{r^2}{R_0^2}\right)^{1/2}}. \tag{2.33}$$

Comparing Equations (2.32) and (2.33), we have that

$$\int_{t_e}^{t_0} \frac{cdt}{a(t)} = \int_{t_e+\delta t_e}^{t_0+\delta t_0} \frac{cdt}{a(t)}. \tag{2.34}$$

Rearranging the integration limits on the right-hand side, we have

$$\int_{t_e+\delta t_e}^{t_0+\delta t_0} \frac{cdt}{a(t)} = \int_{t_e}^{t_0} \frac{cdt}{a(t)} + \int_{t_0}^{t_0+\delta t_0} \frac{cdt}{a(t)} - \int_{t_e}^{t_e+\delta t_e} \frac{cdt}{a(t)}, \tag{2.35}$$

so

$$\int_{t_o}^{t_0+\delta t_0} \frac{cdt}{a(t)} = \int_{t_e}^{t_e+\delta t_e} \frac{cdt}{a(t)}. \tag{2.36}$$

[4] δt_e and δt_0 are infinitesimal.

Thus,

$$\frac{\delta t_0}{a(t_0)} = \frac{\delta t_e}{a(t_e)}. \tag{2.37}$$

In an expanding universe, where $a(t_0) > a(t_e)$, it follows that $\delta t_0 > \delta t_e$ (LIDDLE, 2003).

Considering now a single wave with period δt_e and wavelength $\lambda_e = c\delta t_e$, we find that the emitted photon and the observed photon obey the relation (LIDDLE, 2003; THEUNS, 2021)

$$\frac{\lambda_0}{\lambda_e} = \frac{a(t_0)}{a(t_e)} \equiv 1 + z, \tag{2.38}$$

where z is the *cosmological redshift*.

2.4 Cosmological distances

In cosmology, measuring distance requires taking into account the expansion of the universe and the fact that light takes a finite amount of time to reach the observer. Therefore, considering the FLRW metric, in the following subsections, we will discuss proper distance, comoving distance, luminosity distance, and angular diameter distance.

2.4.1 Proper Distance

The direct implication of the assumption of homogeneity is the existence of a universal cosmic time, t, which allows the same sequence of events in the universe to be viewed by different observers (PETTINI, 2018). As a consequence, it is possible to obtain the distance between two events, A and B, in a reference frame where they occur simultaneously, that is, where $t_A = t_B$. This is referred to as the *proper distance*, $d_p(t)$.

Formally, we can obtain the expression for d_p starting from the FLRW metric (Equation (2.4)),

$$ds^2 = -c^2dt^2 + a^2(t)\left[\frac{dr^2}{1 - k\frac{r^2}{{R_0}^2}} + r^2\left(d\theta^2 + \sin^2\theta d\phi^2\right)\right], \tag{2.39}$$

assuming the condition $d\theta = d\phi = 0$ and, as they are simultaneous events, $dt = 0$, we have,

$$ds^2 = a^2(t)\left[\frac{dr^2}{1 - k\frac{r^2}{{R_0}^2}}\right], \tag{2.40}$$

and

$$d_p(t) = \int_0^s ds' = a(t)\int_0^r \frac{dr'}{\left(1 - k\frac{r'^2}{{R_0}^2}\right)^{1/2}}, \tag{2.41}$$

whose possible solutions depend on the value assumed for k, namely

$$d_p(t) = a(t) \begin{cases} R_0 \sin^{-1}\left(\frac{r}{R_0}\right) & \text{for } k > 0, \\ r & \text{for } k = 0, \\ R_0 \sinh^{-1}\left(\frac{r}{R_0}\right) & \text{for } k < 0. \end{cases} \tag{2.42}$$

Thus, in Euclidean geometry ($k = 0$), the proper distance to an object is equal to its coordinate distance. The same is not true when we have a spherical geometry ($k > 0$), as $\sin^{-1} r > r$, and consequently, the proper distance will be greater than the coordinate distance. Similarly, in hyperbolic geometry, the proper distance will be smaller than the coordinate distance, as $\sinh^{-1} r < r$ (PETTINI, 2018).

2.4.2 Comoving Distance

The proper distance is related to the trajectory of the photon emitted at t_e and observed at t_0, with $ds = d\theta = d\phi = 0$, and

$$d_p(t) = \int_{t_e}^{t_0} \frac{cdt}{a(t)}. \tag{2.43}$$

The information we extract from the spectrum of a galaxy is its redshift, z, which is related to the scale factor through

$$1 + z = \frac{a(t_0)}{a(t)} = \frac{1}{a(t)}, \tag{2.44}$$

where we define $a(t_0) \equiv 1$[5]. Differentiating Equation (2.44) with respect to time t, we have

$$\frac{d(1+z)}{dt} = \frac{d}{dt}\left[\frac{a(t_0)}{a(t)}\right] = -\frac{a(t_0)}{a^2(t)}\frac{da(t)}{dt}. \tag{2.45}$$

Since $a(t_0)$ is a constant, we can simplify further

$$dz = -\frac{\dot{a}(t)}{a^2(t)}dt = -\frac{H(z)}{a(t)}dt, \tag{2.46}$$

With the introduction of the Hubble parameter $H(z) \equiv \dot{a}(t)/a(t)$. This equation relates the rate of change of redshift with respect to time to the rate of change of the scale factor with respect to time. Substituting this expression into Equation (2.43), we have the expression for the comoving distance,

$$d_c = c\int_0^z \frac{dz'}{H(z')}. \tag{2.47}$$

[5]The scale factor is a dimensionless quantity.

This distance is defined in a way that accounts for the expansion of the universe over time, as illustrated in Figure 2.4.

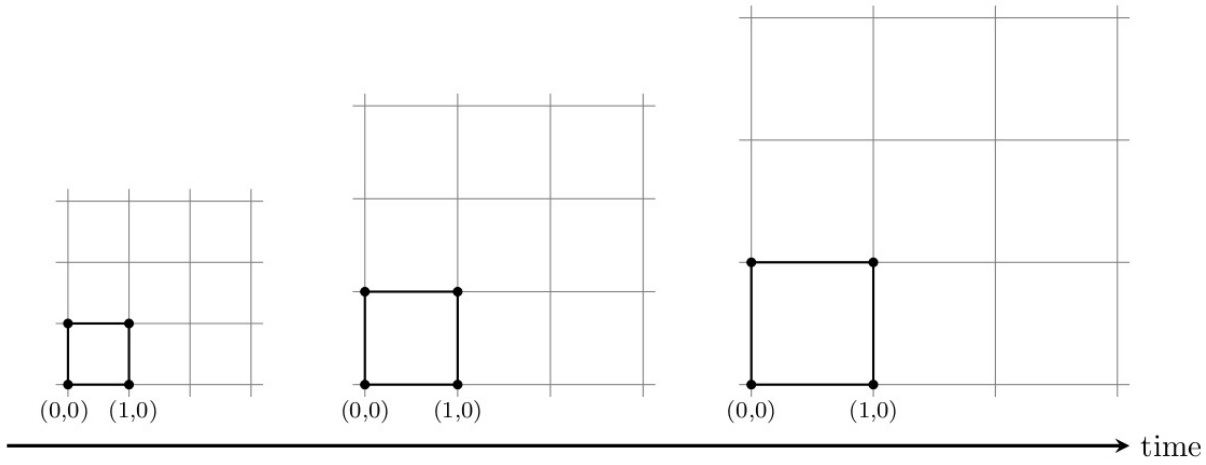

Figure 2.4: The comoving distance between points on an imaginary coordinate grid remains constant as the universe expands (BAUMANN, 2022).

From Equation (2.26), we obtain

$$d_c = c\int_0^z \frac{dz'}{\sqrt{\Omega_{r,0}(1+z')^4 + \Omega_{m,0}(1+z')^3 + (1-\Omega_{m,0}-\Omega_{\Lambda,0})(1+z')^2 + \Omega_{\Lambda,0}}}. \tag{2.48}$$

As the contribution from radiation is negligible, it can be safely disregarded.

2.4.3 Luminosity Distance

When the absolute luminosity of a source, L, is known and the flux, F, can be measured, the distance to that source is obtained using the function known as the *luminosity distance*, d_L,

$$d_L \equiv \left(\frac{L}{4\pi F}\right)^{1/2}. \tag{2.49}$$

Considering the expansion of the universe, this relation needs to be modified. Assuming that photons with wavelength λ_e were emitted in the time interval δt_e, their observation will occur in the time interval δt_0. Given the emission energy of a photon, $h\nu_e = hc/\lambda_e$, as the photon redshifts, the energy will decrease according to $h\nu_0 = h\nu_e/(1+z)$, and consequently, the flux will also decrease (PETTINI, 2018; RYDEN, 2003; THEUNS, 2021). The result for a universe with approximately zero curvature is given by

$$d_L = d_c(1+z) \tag{2.50}$$

2.4.4 Angular Diameter Distance

Assuming a light source with a physical size ℓ, as illustrated in Figure 2.5, we can define the *angular diameter distance*, d_A, as

$$d_A \equiv \frac{\ell}{\delta\theta}. \tag{2.51}$$

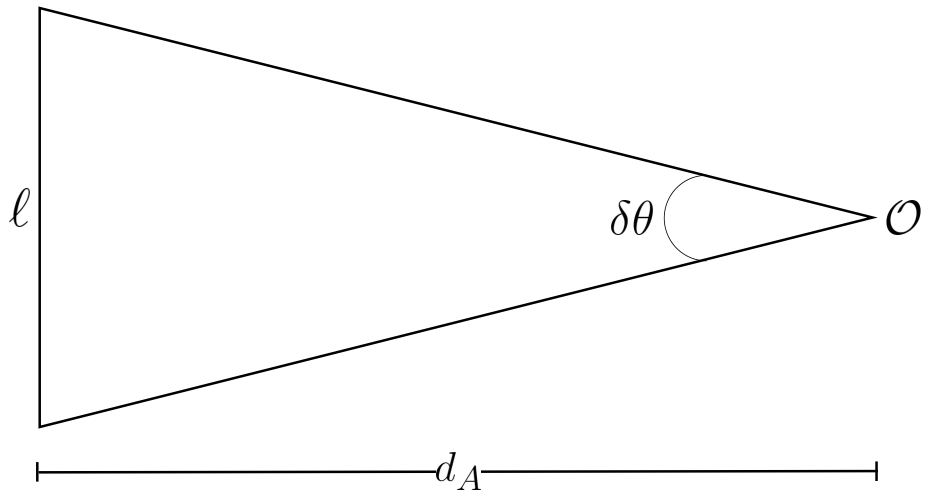

Figure 2.5: The angular diameter distance is the measurement of the angle subtended by the apparent diameter of a luminous source, as seen from an observer located at a fixed point in space. The larger the angle, the greater the angular diameter distance.

This quantity is a way to measure how large objects appear, assuming Euclidean geometry (LIDDLE, 2003). In the case of non-zero curvature, there is a relationship between d_A and the comoving distance (THEUNS, 2021),

$$d_A = \frac{d_c}{1+z}. \tag{2.52}$$

The angular diameter distance is a quantity that can be obtained through observations, unlike the comoving distance.

2.5 Cosmological Observables

Next, we will provide a brief summary of some of the key cosmological observables: the accelerated expansion of the universe, the dark matter, and the cosmic microwave background (CMB).

2.5.1 Accelerated expansion

As seen in Section 2.3.1, our universe is undergoing expansion. However, it remained to be determined what type of expansion it was: constant, accelerated, or decelerated. The answer was only provided seven decades after Hubble's discovery through the independent results obtained by RIESS *et al.* (1998) and PERLMUTTER *et al.* (1999) using Type Ia supernovae: the universe is in a phase of accelerated expansion.

Both studies found that the density parameter Ω_Λ has a non-zero value. Thus, it is necessary to introduce a component with negative pressure in order to account for the accelerated expansion, component known as *dark energy*, into Equation (2.9). However, the nature of this energy, and its modes of interaction, still remain unknown.

2.5.2 Dark matter

In 1933, Fritz Zwicky, studying the Coma Cluster, concluded that in order for the measured line-of-sight velocity dispersion to be compatible with the theory, there must be an additional contributor to the gravitational potential (ZWICKY, 1933). Since it is not known for certain what this contributor is, it has been attributed the name *dark matter*. X-ray observations, gravitational lensing effects, and the analyses of Vera Rubin of galaxy rotation curves (RUBIN *et al.*, 1980, 1985) support this evidence.

Dark matter is expected to be composed of particles that do not interact with photons, and several candidates are being studied. One of these candidates are neutrinos, which are relativistic particles with extremely small mass. The problem with these particles is that they would lead to a scenario where larger structures formed before smaller ones, being part of the hypothesis known as *hot dark matter* (HDM), which is inconsistent with observations. Another possibility is the *cold dark matter* (CDM) hypothesis, composed of non-relativistic particles that allow the formation of structures as predicted by the theory (i.e., during the matter-dominated era).

2.5.3 Cosmic Microwave Background Radiation (CMB)

In the primordial universe, there was a phase of thermal equilibrium between matter and radiation. With expansion, the photons that were once tightly coupled to baryons and electrons become less energetic, and nuclei can capture electrons to form hydrogen. Over time, the scattering rate of photons by electrons becomes smaller than the expansion rate of the universe, until the last scattering occurs. At this moment, the universe ceases to be opaque and becomes transparent, with photons traveling freely, giving rise to the Cosmic Microwave Background (CMB).

The CMB is an electromagnetic radiation detected in the microwave range of the spectrum and was discovered by Penzias and Wilson in 1965. This radiation is still present

today, with a temperature T_0 today, and its energy distribution is perfectly described by a blackbody spectrum, as shown in Figure 2.6.

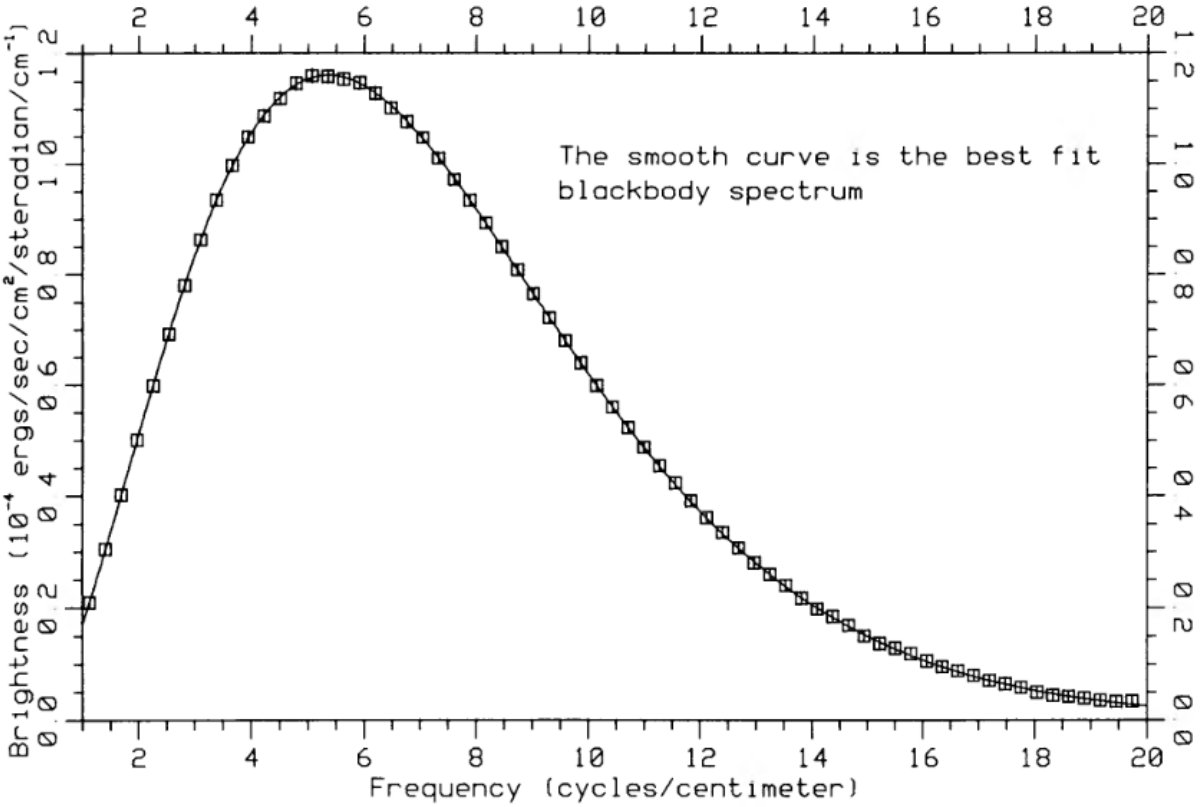

Figure 2.6: Spectrum of the cosmic microwave background radiation with data obtained by the COBE satellite (MATHER *et al.*, 1990).

The Far InfraRed Absolute Spectrophotometer (FIRAS) experiment, launched in 1989 aboard the COsmic Background Explorer (COBE) satellite, verified that the temperature of the CMB is (FIXSEN *et al.*, 1996; MATHER *et al.*, 1990)

$$T_0 = 2.728 \pm 0.004\text{K}. \tag{2.53}$$

The WMAP (Wilkinson Microwave Anisotropy Probe; HINSHAW *et al.* (2013)) satellite and the Planck (PLANCK COLLABORATION *et al.*, 2020a) satellite obtained a temperature (FIXSEN, 2009)

$$T_0 = 2.72548 \pm 0.00057\text{K}. \tag{2.54}$$

The COBE data also revealed the presence of a dipole with an amplitude of 3.353 ± 0.024 mK in the direction $(\ell, b) = (264^\circ.26 \pm 0.33^\circ, 48^\circ.2 \pm 0.13^\circ)$. This dipole is a consequence of the non-isotropic nature of the Local Universe, caused by the relative motions of galaxies that affect the measurement of the CMB temperature given a net motion of our galaxy in that direction.

In addition to the monopole and dipole components, the CMB map shows tiny temperature fluctuations that have been used to test the statistical isotropy hypothesis (ALURI and SHAFIELOO, 2017; ALURI *et al.*, 2017; BERNUI and HIPÓLITO-RICALDI, 2008; BERNUI *et al.*, 2006, 2007, 2014; BERNUI, 2008, 2009; HANSEN *et al.*, 2004; PLANCK COLLABORATION *et al.*, 2020b; POLASTRI *et al.*, 2015; RASSAT *et al.*, 2014).

Chapter 3

Data selection and synthetic catalogs

In this Chapter, we will present the data used in our analysis to study the statistical isotropy in the Local Universe. In Section 3.1, we will provide a brief description of the properties of the observational data catalog. Subsequently, in Section 3.2, we will explain the creation of the synthetic catalogs, needed to estimate the values of the correlation function and estimate the uncertainties of the measurements.

3.1 Observational data: the ALFALFA catalog

To study the statistical isotropy in the Local Universe, $z \lesssim 0.06$, we utilized the ALFALFA catalog (Arecibo Legacy Fast ALFA Survey)[1]. The ALFALFA dataset was chosen due to its convenient properties, which include: (i) a good number density ($n \sim 4\,\mathrm{deg}^{-2}$); (ii) a large survey area of approximately $\sim 7000\mathrm{deg}^2$ or $\sim 1/6$ of the sky, allowing for the division of the sky into multiple appropriately sized patches; and (iii) the relative bias of the HI sources, with respect to matter, is close to that of blue galaxies (AVILA *et al.*, 2018; PAPASTERGIS, 2013), which, in turn, is ~ 1 (AVILA *et al.*, 2019; CRESSWELL and PERCIVAL, 2009). These characteristics make the HI sources interesting cosmic tracers of (dark) matter in the Local Universe.

3.1.1 General characteristics

The ALFALFA catalog was a survey that detected 31502 extragalactic HI line sources, in 21 cm, between the years 2005 and 2012, with the complete version ($\alpha.100$) made available in 2018 (HAYNES *et al.*, 2018; JONES *et al.*, 2016). These objects are located in the Local Universe, within the redshift range of $0 < z < 0.06$ (*vide* the redshift histogram in Figure 3.1).

The ALFALFA's footprint covers $\sim 7000\,\mathrm{deg}^2$ of the sky, with $\sim 4500\,\mathrm{deg}^2$ in the northern Galactic hemisphere (NGH or Spring) and $\sim 2800\,\mathrm{deg}^2$ in the southern Galactic

[1] http://egg.astro.cornell.edu/alfalfa/data/index.php

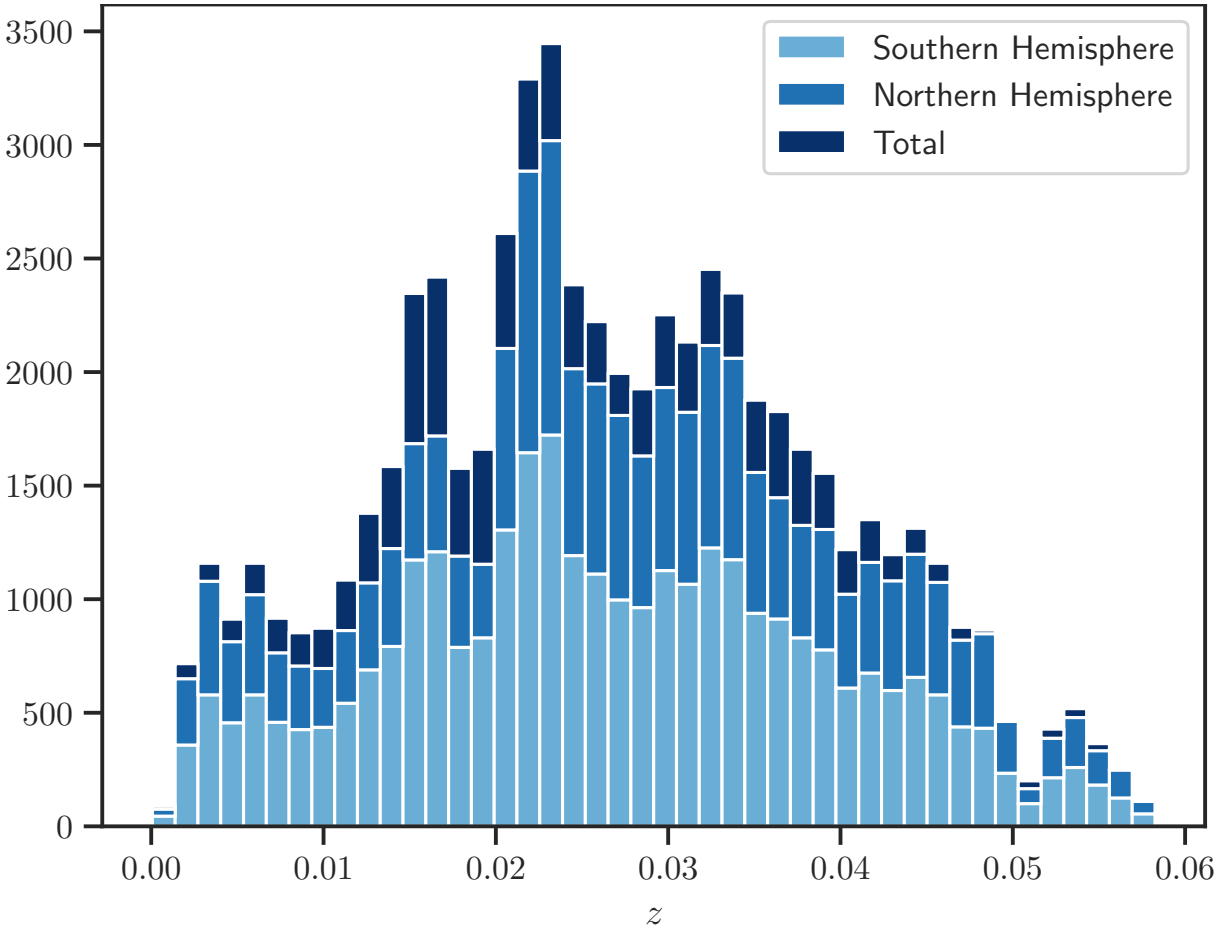

Figure 3.1: The histogram presents the distribution of redshifts for the ALFALFA data. It illustrates the frequency of sources at different redshift intervals within the range of $0 < z < 0.06$.

hemisphere (SGH or Fall). Both hemispheres lie within the declination range of $0^\circ < \delta < 36^\circ$, with the NGH covering the region of right ascensions between $7^h20^m < \alpha < 16^h40^m$, and the SGH covering the region between $21^h30^m < \alpha < 3^h15^m$. Out of the total number of objects, 21578 are located in the NGH, while 9924 are in the SGH, as illustrated in Figure 3.2.

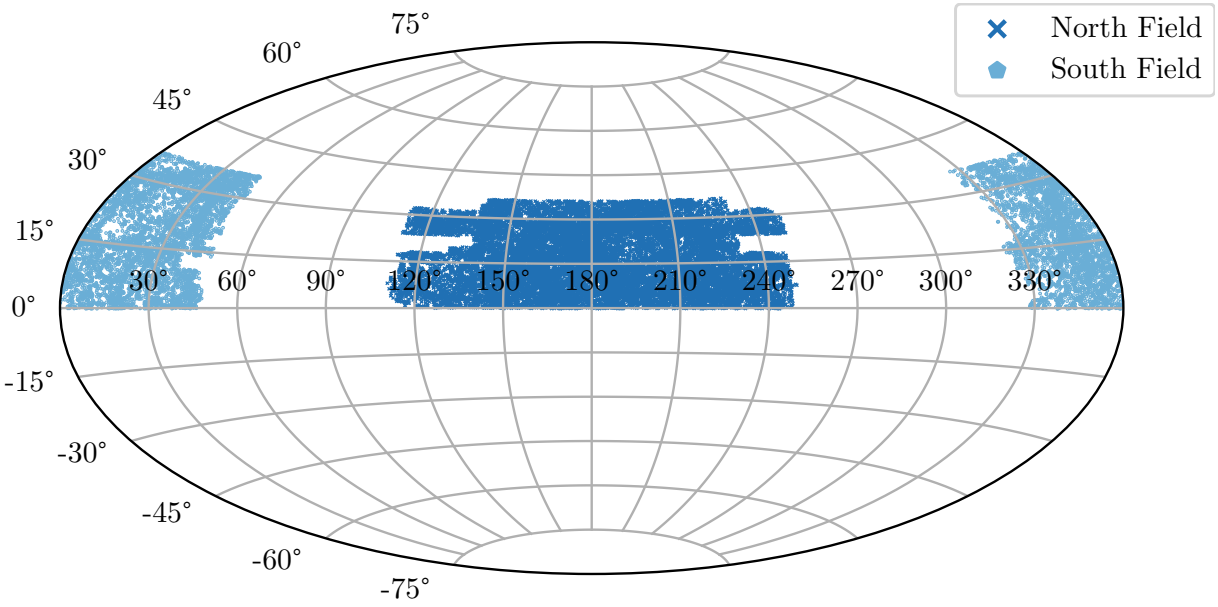

Figure 3.2: Footprint of the ALFALFA catalog in equatorial coordinates. The central region corresponds to the southern Galactic hemisphere, while the regions at the extremes, together, correspond to the northern Galactic hemisphere.

The data were classified as either CODE 1 or CODE 2 according to criteria established by the ALFALFA collaboration team (HAYNES *et al.*, 2018). One of these criteria is the signal-to-noise ratio (SNR). If the source is associated with an optical counterpart (OC) with comparable redshift and has SNR > 6.5, it is classified as CODE 1. Sources that coincide with an OC but have SNR $\lesssim 6.5$ are considered as CODE 2. CODE 1 sources are nearly 100% reliable (HAYNES *et al.*, 2018).

3.1.2 Selection criteria

Following the recommendation of the ALFALFA team, we only considered sources classified as CODE 1. Consequently, our sample consisted of 16285 and 9149 reliable sources in the NGH and SGH, respectively.

Next, the hemispheres were subdivided to maximize the number of regions with a sufficient minimum size to avoid statistical noise dominance, clustering, or voids. For this purpose, we adopted a minimum scale for quadrilaterals greater than 20° (AVILA *et al.*, 2019). As a result, we obtained ten regions for analysis: six in the NGH and four in the SGH (*vide* Figure 3.3).

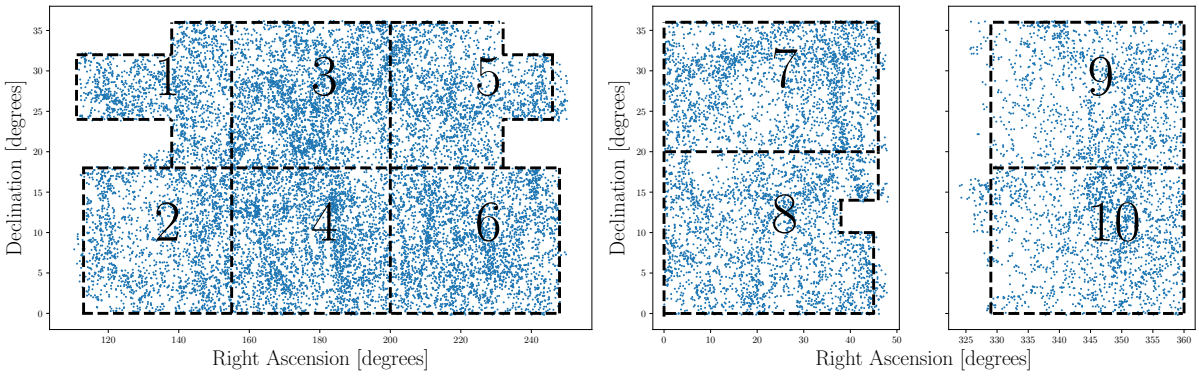

Figure 3.3: ALFALFA footprint division in 10 sky patches for statistical isotropy analyses using the two-point angular correlation function. The regions 1–6 and 7–10 correspond to the Spring and Fall regions, respectively.

It is important to note that each region was carefully delimited to avoid excessively irregular shapes that could compromise the reproducibility of the analyzed footprint. In order to ensure this condition, a few additional points were removed, resulting in our final sample of 15993 HI clouds in the NGH and 8828 clouds in the SGH. The features of each region can be found in Table 3.1 and in Figure 3.3.

Table 3.1: The properties of the ten analyzed regions are as follows. It is important to note that the most significant characteristic of each region is its number density, with an average value of $\overline{n} \simeq 3.42\,\mathrm{deg}^{-2}$. The uncertainties were calculated using $\sigma_n = \sqrt{N}/\mathrm{area}$, where N is the number of sources.

	Sources	Area [deg^2]	n [deg^{-2}]
Area 1	1648	522	3.15 $\pm$ 0.08
Area 2	2081	756	2.75 $\pm$ 0.06
Area 3	3372	810	4.16 $\pm$ 0.07
Area 4	3427	810	4.23 $\pm$ 0.07
Area 5	2157	688	3.13 $\pm$ 0.07
Area 6	3308	864	3.83 $\pm$ 0.07
Area 7	2474	736	3.36 $\pm$ 0.07
Area 8	2844	875	3.25 $\pm$ 0.06
Area 9	1636	558	2.93 $\pm$ 0.07
Area 10	1874	558	3.36 $\pm$ 0.08

Despite the differences in the number of sources and area in each region, our concern was to maintain the number densities, n, i.e., the number of objects per unit area, approximately equal.

3.2 Synthetic catalogs

In our analyses, we utilized two types of synthetic catalogs: *random* and *mock* catalogs. The random catalogs were employed to estimate the two-point correlation function, which

will be discussed in Section 4.1. On the other hand, the mock catalogs were used to estimate the uncertainties associated with our measurements, as described in Section 4.2. The detailed construction of both types of synthetic catalogs will be presented in Subsections 3.2.1 and 3.2.2.

3.2.1 Random catalogs

In this work, a random catalog refers to a set of pseudo-randomly generated ordered pairs, that are uniformly distributed over a specified range in right ascension and declination. These catalogs reproduce the analyzed region, i.e., they have the same ranges in right ascension and declination and the same number of points. For each region presented in Figure 3.3, 25 catalogs of this type were generated, following the procedure described by BERNUI *et al.* (2004) (see also DE CARVALHO *et al.* (2018); DE CARVALHO (2019); KEIHÄNEN *et al.* (2019); PAPASTERGIS (2013); WANG *et al.* (2013)). In this way, given a random number R_i in a range $\Delta\delta'$, the declinations will be

$$\delta_i = \arcsin R_i \,. \tag{3.1}$$

The right ascensions are the values selected from a uniform distribution within the range $\Delta\alpha'$. An illustrative comparison between the footprint of one of the regions and its respective random catalog can be observed in Figure 3.4.

3.2.2 Log-normal mocks catalogs

To estimate the uncertainties of our results (further details in Chapter 4), we used log-normal catalogs (mocks). This is necessary due to the underestimation of errors when using a random catalog for this purpose (DE CARVALHO *et al.*, 2018, 2020; NORBERG *et al.*, 2009).

The current scenario is to assume a Gaussian random field to describe $\tilde{\delta}(\mathbf{x})$ because (i) it is predicted by most inflationary models (see BARROW and COLES (1990) and references therein) and (ii) the model is fully specified, i.e., statistically complete (COLES and JONES, 1991)[2]. Thus we need only the 2-point correlation function $\xi(r)$, or its Fourier transform $P(k)$, to describe the matter density field (AGRAWAL *et al.*, 2017).

However, Gaussian random fields cannot describe the matter distribution, it assigns non-zero probability for negative densities (FRY, 1986). Although small in the beginning, the matter fluctuations grow as gravitational instability takes over, thus it cannot describe consistently the non-linear density matter distribution at late times. This motivates the construction of *stochastic models* for the density field: models which are completely

[2]Gaussian random fields are completely determined once we specify the following two functions, the mean and the covariance (ADLER, 2010).

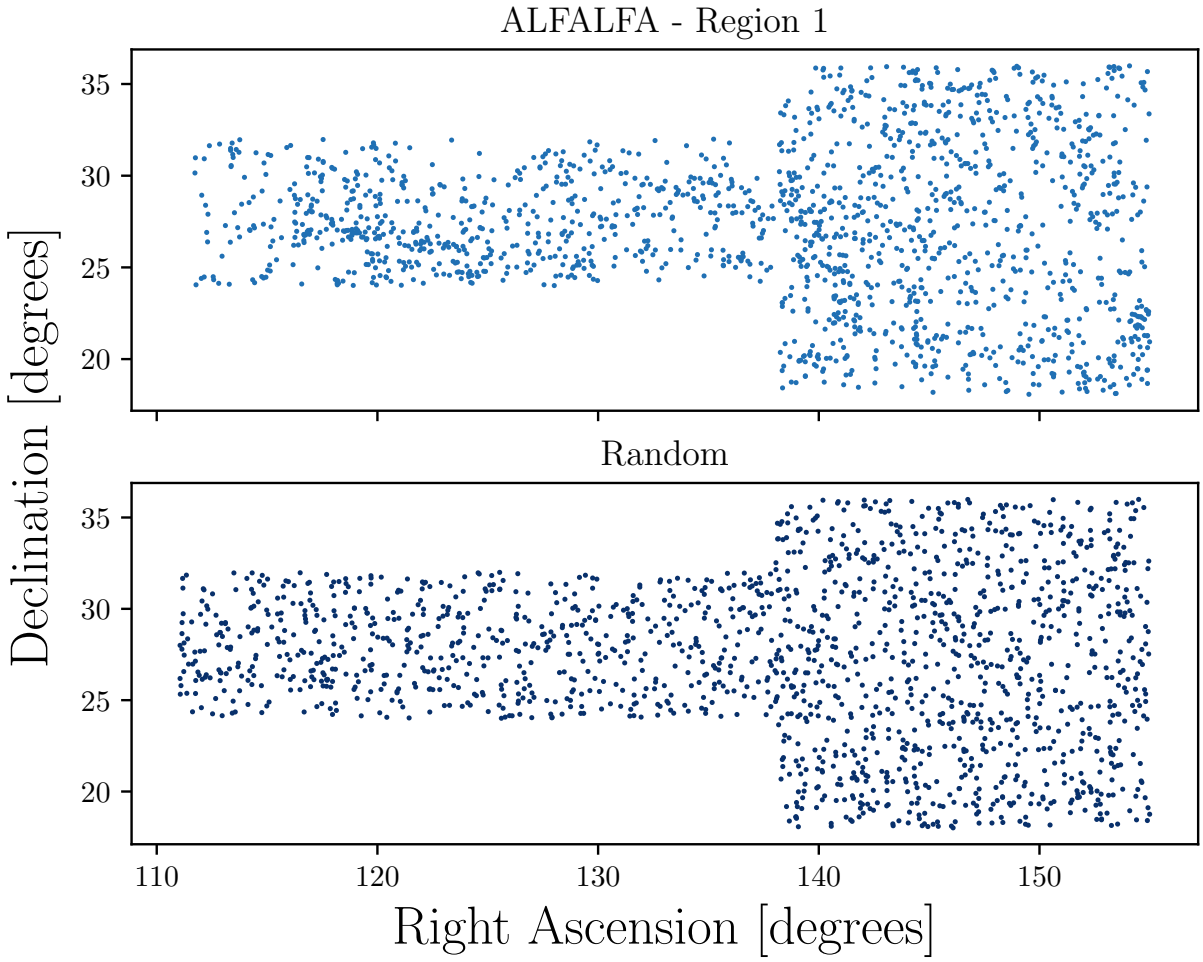

Figure 3.4: Comparison between a random catalogue and the data cut corresponding to Area 1 of the ALFALFA catalog.

Table 3.2: The survey configuration used to generate a set of 1000 log-normal mock catalogs for our analyses.

Survey configuration
$z = 0.0$
$b = 1.0$
$N_g = 2 \times 10^5$
$L_x = 230$ Mpc/h
$L_y = 230$ Mpc/h
$L_z = 230$ Mpc/h

Table 3.3: Latest cosmological parameters available from PLANCK COLLABORATION *et al.* (2020a).

Cosmological parameters
$\Omega_b h^2 = 0.02236$
$\Omega_c h^2 = 0.1202$
$\ln(10A_s) = 3.045$
$n_s = 0.9649$
$\Sigma m_\nu = 0.06$ eV
$h = 0.6727$

specified statistically but do not violate $\rho > 0$ (COLES and JONES, 1991).

One model that happen to fulfill these two conditions is the log-normal random field (BERNARDEAU and KOFMAN, 1995; COLES and JONES, 1991; COLOMBI, 1994; KOFMAN *et al.*, 1994; SHIN *et al.*, 2017; UHLEMANN *et al.*, 2016).

We generated a set of 1000 mocks using the public code[3] developed by AGRAWAL *et al.* (2017). Each catalog represents a realization of the input parameters provided beforehand, which should align with the characteristics of the data catalog, as listed in Table 3.2.

The mean and median of the redshift distribution, shown in Figure 3.1, are $\langle z \rangle \sim 0.026$. Therefore, we opted for the approximation $z \simeq 0$. The value of the bias, b, has been previously calculated by AVILA *et al.* (2021) based on the results of MARTIN *et al.* (2012). The number of galaxies, N_g, as well as the dimensions of the box [4] (L_x, L_y, L_z), were chosen in order to obtain a similar number density as that of the ALFALFA catalog.

In addition to those, the code requires the cosmological parameters to be adopted in the simulation. We use the results presented in Table 2 of PLANCK COLLABORATION *et al.* (2020a), which are shown in Table 3.3.

The parameters $\Omega_b h^2$ and $\Omega_c h^2$ represent the baryon and cold dark matter densities, respectively; A_s corresponds to the primordial comoving curvature power spectrum amplitude, which quantifies the overall level of density fluctuations in the early universe;

[3] https://bitbucket.org/komatsu5147/lognormal_galaxies/src/master/
[4] in units of Mpc/h

n_s is the scalar spectral index, indicating the tilt or slope of the primordial curvature power spectrum – it provides information about the scale dependence of density fluctuations; Σm_ν represents the sum of the masses of neutrinos; h is the dimensionless Hubble constant, defined by $H_0 \equiv 100h\,\mathrm{km\,s^{-1}\,Mpc^{-1}}$.

An ilustrative example of a mock catalog is shown in Figure 3.5. It can be observed that the distribution is more clustered in some parts than in others, which is expected due to the formation of structures (in this case, described by the fiducial model assumed, i.e., the ΛCDM model).

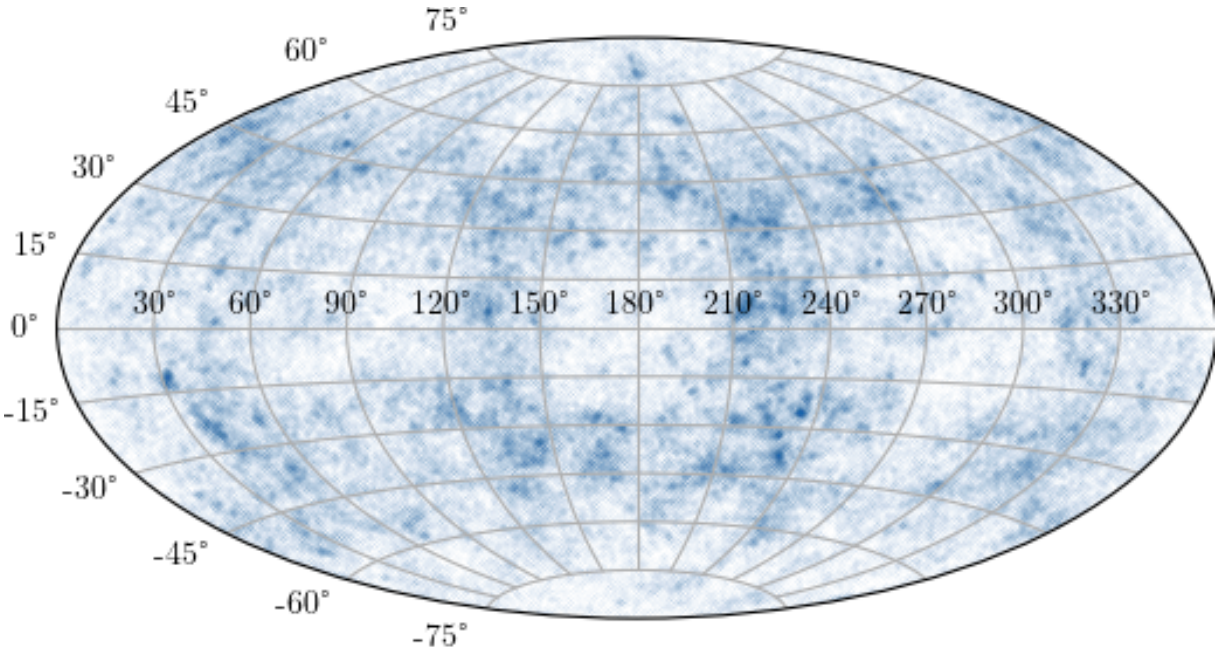

Figure 3.5: Example of a log-normal mock catalog. The points are distributed throughout the entire sky according to the expected distribution from the concordance model.

With the generated set of mocks, we cut out each of the regions in Figure 3.3 in the same manner as described in Subsection 3.1.1, i.e., maintaining the footprint and the number of points in each region[5]. This resulted in samples such as the one illustrated in Figure 3.6.

[5]Due to the nature of the simulation, the number of objects in each realization fluctuates. Therefore, after the region cutout, we randomly selected objects in an effort to have equivalent quantities to the data for each region in analysis.

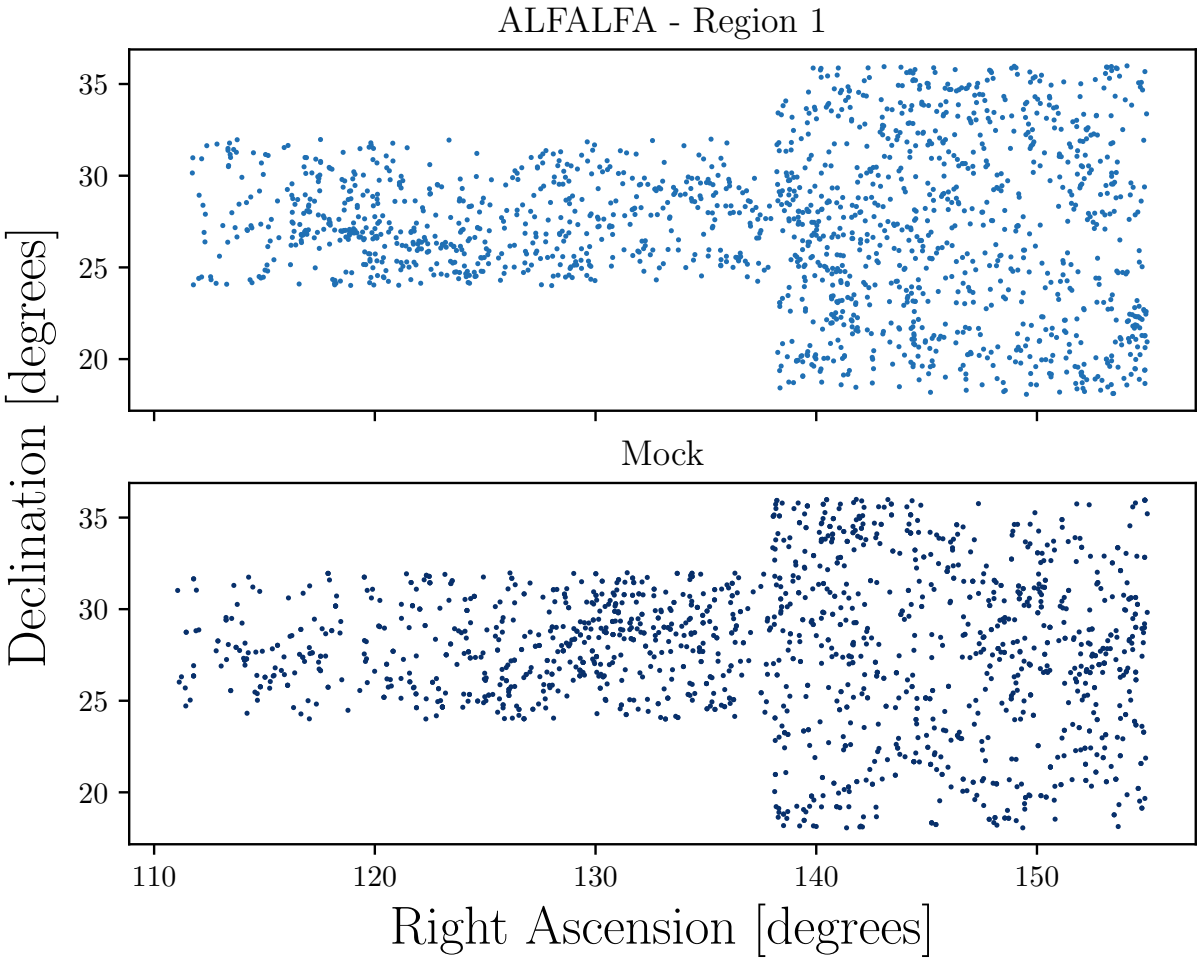

Figure 3.6: Comparison between a mock catalogue and the data cut corresponding to Area 1 of the ALFALFA catalog.

Chapter 4

Statistical methods

In studies involving the large-scale structure of the universe, the use of the two-point correlation function (2PCF) is convenient for quantifying the clustering of matter, in addition to being subject to interpretation. The three-dimensional version of the 2PCF requires the assumption of a cosmological model to convert angular coordinates and redshift into distances (DE CARVALHO, 2019; PEEBLES, 1993). However, we only use measurements of right ascension (RA or α) and Declination (DEC or δ), and, therefore, our analyses are independent of a cosmological model. As a result, this work is based on the projected version of the two-point correlation function, known as the two-point *angular* correlation function (2PACF).

4.1 Two-Point Angular Correlation Function (2PACF)

Assuming a collection of N randomly distributed points in a volume V, the probability of finding a point centered in the infinitesimal volume dV is given by

$$dP = \frac{N}{V} dV = n dV, \tag{4.1}$$

where $n = N/V$ is the number density of points in the region (LIMA NETO, 2022; PEEBLES, 1993). If there are two objects, the joint probability of finding them in volumes dV_1 and dV_2, respectively, is given by

$$dP = (n dV_1)(n dV_2) = n^2 dV_1 dV_2. \tag{4.2}$$

The Equations (4.1) and (4.2) do not quantify clustering as they are independent of the distance between objects. In this case, we need to use the two-point correlation function ($\xi(r)$, 2PCF), which is defined by the joint probability of finding an object in both of the

volume elements dV_1 and dV_2 (PEEBLES, 1981),

$$dP \equiv n^2[1 + \xi(r)]dV_1 dV_2, \tag{4.3}$$

with r being the distance between pairs of objects, measured in units of h^{-1}Mpc, and n representing the mean number density of the sample (COIL, 2013; LIMA NETO, 2022; PEEBLES, 1993).

The correlation function can also be determined solely based on the projected positions of objects (RA and DEC). Thus, we have the two-point angular correlation function, ($\omega(\theta)$ or 2PACF), which is defined similarly to Equation (4.3),

$$dP \equiv n^2[1 + \omega(\theta)]d\Omega_1 d\Omega_2\,, \tag{4.4}$$

where $d\Omega$ is the solid angle element of a cosmic object at an angular separation θ from a second galaxy. This angular separation is calculated using

$$\theta_{ij} = \cos^{-1}[\sin(\delta_i)\sin(\delta_j) + \cos(\delta_i)\cos(\delta_j)\cos(\alpha_i - \alpha_j)], \tag{4.5}$$

where α_i, α_j, δ_i, and δ_j are the right ascension and declination, respectively, of the objects i and j.

In practice, the correlation function uses estimators based on counting pairs of objects as a function of distance. There are several estimators in the literature (DAVIS and PEEBLES, 1983; HAMILTON, 1993; HEWETT, 1982); the most used are the Peebles-Hauser estimator (PH; PEEBLES and HAUSER (1974)).

$$\omega_{PH}(\theta) = \frac{DD(\theta)}{RR(\theta)} - 1, \tag{4.6}$$

and the Landy-Szalay estimator (LS; LANDY and SZALAY (1993)),

$$\omega_{LS}(\theta) \equiv \frac{DD(\theta) - 2DR(\theta) + RR(\theta)}{RR(\theta)}\,, \tag{4.7}$$

where $DD(\theta)$, $RR(\theta)$ and $DR(\theta)$ are the number os pairs of cosmic objects normalized by the total number of pairs as follows:

$$DD(\theta) = \frac{dd(\theta)}{[N_d(N_d - 1)/2]}\,, \tag{4.8}$$

$$RR(\theta) = \frac{rr(\theta)}{[N_r(N_r - 1)/2]}\,, \tag{4.9}$$

$$DR(\theta) = \frac{dr(\theta)}{N_d N_r}, \tag{4.10}$$

where $dd(\theta)$ is the number of pairs of cosmic objects in the data catalog with angular separation θ; $rr(\theta)$ is a similar quantity, but for pairs in the synthetic catalog; and $dr(\theta)$ corresponds to a cross-correlation between an object in the data and an object in the synthetic catalog (LANDY and SZALAY, 1993; PEEBLES and HAUSER, 1974; VARGAS-MAGAÑA *et al.*, 2013).

Three cases are possible for $\omega(\theta)$:

$$\omega(\theta) \begin{cases} < 0\,, & \text{segregated distribution (negative correlation)} \\ = 0\,, & \text{Poisson distribution (random)} \\ > 0\,, & \text{clustered distribution (positive correlation)} \end{cases} \tag{4.11}$$

The case where $\omega(\theta) < 0$ indicates that is less likely to found pairs at a given angular distance θ, indicating a tendency for objects to be more dispersed or anti-clustered in the universe. The second one, $\omega(\theta) = 0$, suggests no correlation between the cosmic objects at the given angular separation θ; this indicates a random or uniform distribution of objects, without any preferential clustering or agglomeration. Lastly, when $\omega(\theta) > 0$, the objects are more likely to be found together in pairs or groups, indicating a clustering of matter in the sample in analysis. If we have a sample that is homogeneous on large scales, then, for every interval of the angular scale θ where $\omega(\theta) > 0$, there will be a complementary interval where $\omega(\theta) < 0$ (LIMA NETO, 2022).

The most intuitive estimator –in physical terms– is the PH estimator, which directly compares the count of data pairs and random pairs to unity (PAPASTERGIS, 2013); on the other hand, although the LS estimator requires more computational time, it exhibits better statistical performance and is less sensitive to the size of the random catalog (COIL, 2013; KERSCHER *et al.*, 2000).

Unless explicitly stated, in our analyses we calculate the 2PACF using 80 bins linearly spaced between 0.01° and 40° for large-scale analyses, and 20 bins in the linear interval between 0.01° and 10° for small-scale analyses.

It is expected that the 2PACF behaves according to a power-law function (COIL, 2013; CONNOLLY *et al.*, 2002; KURKI-SUONIO, 2023; MARQUES and BERNUI, 2020; PEEBLES, 1993; TOTSUJI and KIHARA, 1969). Therefore, after estimating the 2PACF, we plot the best-fit curve using the Equation

$$\omega(\theta) = \left(\frac{\theta}{\theta_0}\right)^{-\beta}, \tag{4.12}$$

where the parameter θ_0 is the transition parameter between the linear and non-linear regimes, and the parameter β quantifies the clustering of matter in the analyzed region

(i.e., the higher the value of this parameter, the closer the galaxies are to each other).

4.2 Estimation of uncertainties

The random catalogs we used to calculate the 2PACF are not considered satisfactory for estimating the uncertainties associated with the calculation of the 2PACF, leading to underestimated values (DE CARVALHO *et al.*, 2018; NORBERG *et al.*, 2009). To overcome this issue, we use the mocks described in Section 3.2.

The procedure followed the description provided by DE CARVALHO *et al.* (2021); MYERS *et al.* (2005); WANG *et al.* (2013). After calculating the 2PACF for a set of N_b bins using the 1000 mocks and the 25 pre-generated random catalogs, we computed the elements of the covariance matrix according to

$$\mathrm{Cov}_{ij} = \frac{1}{N}\sum_{k=1}^{N}[\omega_k(\theta_i) - \overline{\omega}_k(\theta_i)][\omega_k(\theta_j) - \overline{\omega}_k(\theta_j)], \tag{4.13}$$

where the indices $i, j = 1, 2, ..., N_b$ represent each bin θ_i; ω_k is the 2PACF for the k-th mock ($k = 1, 2, ..., N$); $\overline{\omega}(\theta_i)$ and $\overline{\omega}(\theta_j)$ are the mean values for bins i and j, respectively. The uncertainty of $\omega(\theta_i)$ is the square root of the main diagonal of Equation (4.13), $\Delta\omega(\theta_i) = \sqrt{\mathrm{Cov}_{ii}}$.

In order to assess the degree of independence between the bins, we calculate the elements of the correlation matrix using the relationship

$$\mathrm{Corr}_{ij} = \frac{\mathrm{Cov}_{ij}}{\sigma_i \sigma_j}, \tag{4.14}$$

where σ_i, σ_j are the standard deviations of bins i, j, respectively (WASSERMAN, 2004).

In Figure 4.1 we show the correlation matrix for 100 log-normal mocks. It is worth noting that the color scale indicates whether the bins are independent ($\mathrm{Corr}_{ij} = 0$) or whether increasing bin i causes an increase or decrease in bin j ($\mathrm{Corr}_{ij} = +1$ or $\mathrm{Corr}_{ij} = -1$, respectively).

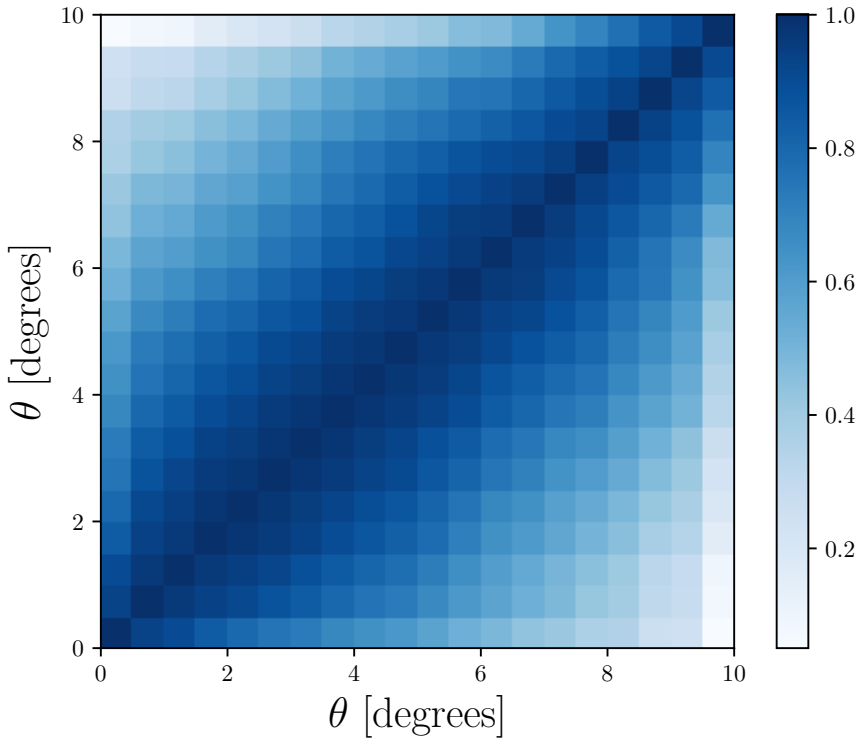

Figure 4.1: Correlation matrix for 100 log-normal mocks obtained from Equation (4.14).

Chapter 5

Results and discussions

With the statistical tools on hands, described in the Chapter 4, we perform the statistical isotropy analyses on the ALFALFA data. First, we perform the 2PACF analyses for our sample –carefully fragmented in 10 directions– to probe the Local Universe isotropy. Next, we discuss the interesting features observed in these 2PACF, like the possible presence of *low-density* structures in some analysed regions. We consider small and large angular analyses in the fitting procedure of the 2PACF; the first one because of the criteria established in the literature (WANG *et al.*, 2013), while the second one is due to the intriguing structures observed, in Figure 5.1, only in some regions at large angles.

5.1 Statistical isotropy analyses with the 2PACF

After some tests we select for analyses 10 regions. For this we divide the ALFALFA footprint into 10 sky patches of $\sim 750\,\mathrm{deg}^2$ each one, six in the Spring region and four in the Fall region, as shown in Figure 3.3, with geometric details specified in Table 3.1. Using the LS estimator, we then calculate the 2PACF, $\omega(\theta)$, for the range $0^\circ < \theta < 40^\circ$, with 80 bins, in each sky patch. Then we perform a best-fit procedure assuming a power-law behavior in the form of Equation (4.12), considering two situations: (i) for small angular scales $\theta \in [0^\circ, 10^\circ]$; and (ii) for large angular scales $\theta \in [0^\circ, 30^\circ]$. The summary of our 2PACF analyses can be seen in Figure 5.1. Notably, some regions show a dissimilar 2PACF at large-angles, interesting results that deserve close inspection.

Furthermore, the best-fit analyses at small and large scales, $\theta_0^{S,L}$ and $\beta^{S,L}$, deserve a comment. The analyses for small angles, $0^\circ < \theta < 10^\circ$, provides a measure of non-linear clustering in the selected 10 sky directions that we compare with 1000 Area-mocks[1] produced under the homogeneity and isotropy hypotheses. This comparison is intended to reveal possible deviations of the best-fit parameters from the 10 ALFALFA regions with respect to the isotropic mocks, simulated data that take into account the clustering

[1] That is, 100 mocks where we consider in each one 10 regions with equal footprint as in Figure 3.3.

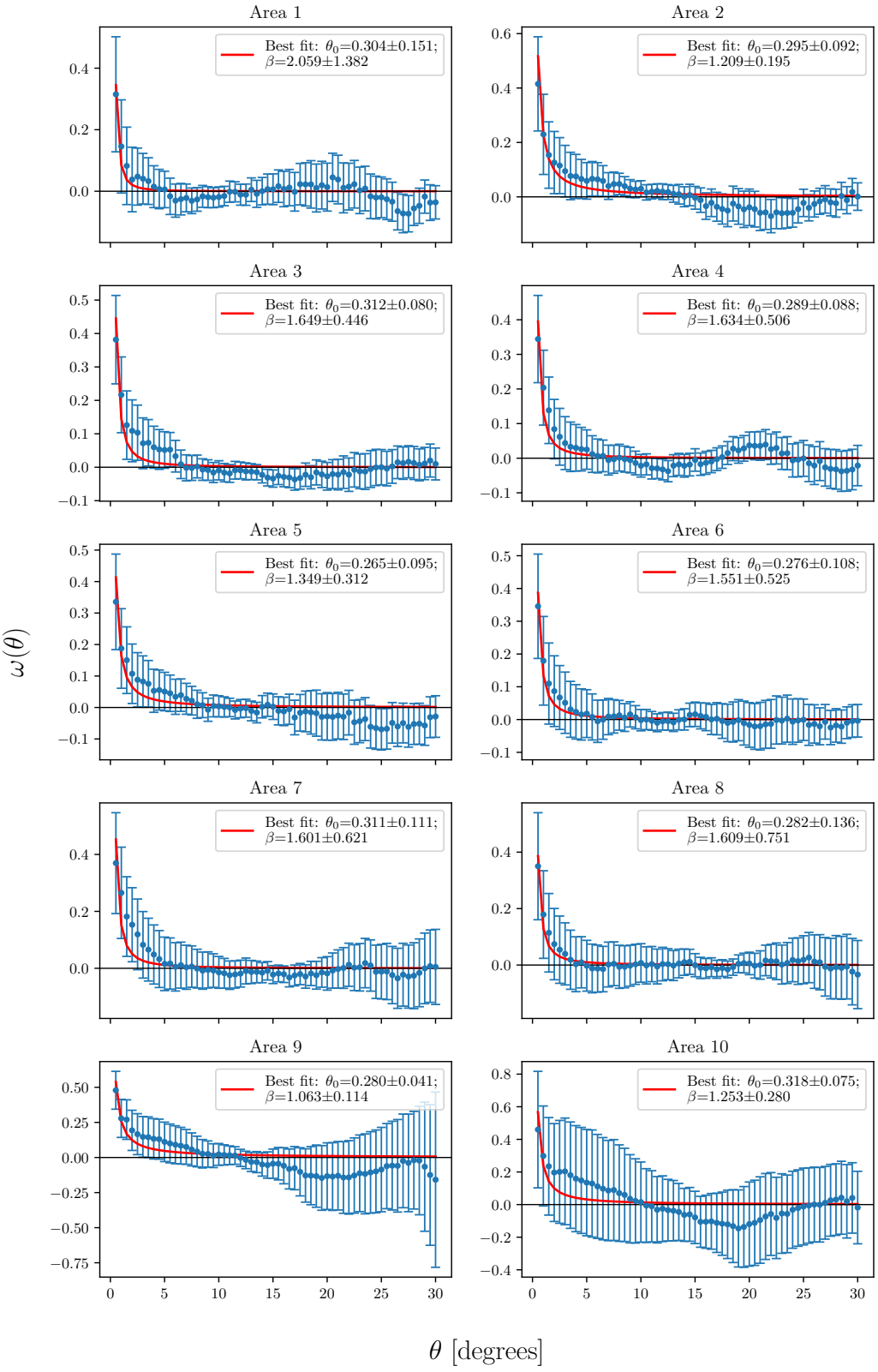

Figure 5.1: Mosaic of the 2PACF for *large-angle analysis*: angular distribution study of the 10 sky patches in which we divide the ALFALFA footprint. We use the 2PACF with the LS estimator for a large angular interval, i.e., $0^\circ < \theta < 30^\circ$. See Section 5.2 for a detailed discussion of the features observed in these 2PACF plots.

evolution of the low-redshift universe. For small-angle analyses, the median value of the best-fit parameter β^S from these 1000 Area-mocks is $\beta^{S;SI} = 1.180 \pm 0.325$, meaning that the 10 sky regions analysed are compatible with the hypothesis of statistical isotropy (SI) within 1.4σ CL. This conclusion can also be seen in the histogram shown in Figure 5.2.

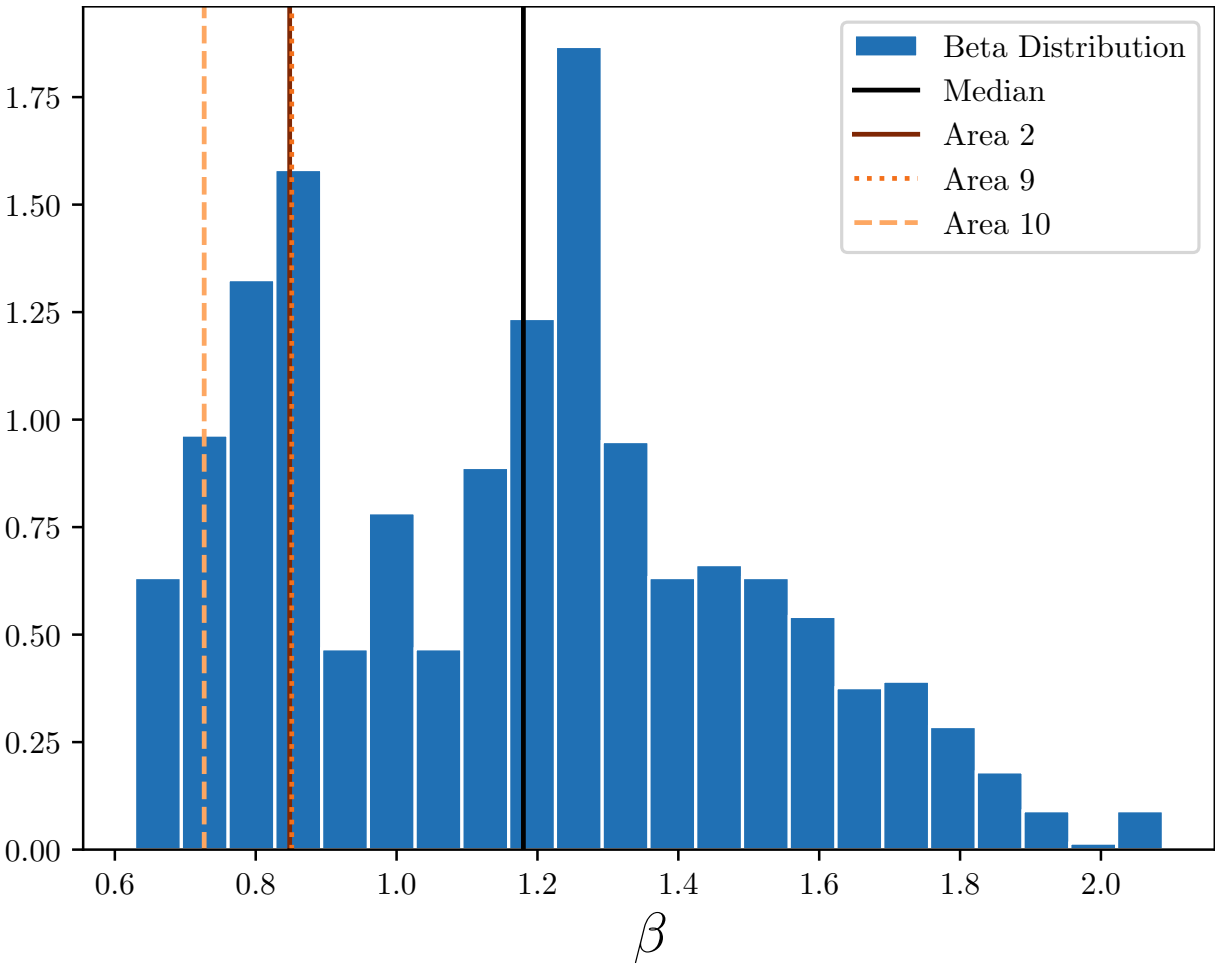

Figure 5.2: Distribution of the best-fit parameter β^S from small-angle analyses of 1000 Area-mocks, the median value is $\beta^{S;SI} = 1.180 \pm 0.325$, meaning that the 10 sky regions analysed are compatible with the hypothesis of statistical isotropy (SI). The values for the Areas 2, 9, and 10 are plotted as continuous, dotted, and dashed vertical lines, respectively (their corresponding β values can be seen in Table 5.1).

From other side, our analysis for large angles, $0^\circ < \theta < 30^\circ$, is intended to reveal features, or structures, besides the 2D homogeneity scale, $\theta_H \simeq 16^\circ$, of the ALFALFA catalog (AVILA *et al.*, 2018). In this case, the best-fit parameters provides partial information, as the 2PACF signatures were more revealing. In fact, we observe that the 2PACF of some regions show a consistent lack of large-angle correlations, manifested in the form of depressions, interesting signatures that motivates us to investigate what could be causing them (analyses that we perform in the next Subsections).

Table 5.1: Best-fit parameters considering the power-law relationship: $\omega(\theta) = (\theta/\theta_0)^{-\beta}$. We have performed two best-fit analyses, for small angles (i.e., $0^\circ < \theta < 10^\circ$) and for large angles (i.e., $0^\circ < \theta < 30^\circ$); we differentiate these cases with the superindex letter S or L. For small angles study the mean for these 10 regions is $\langle\beta\rangle^S = 1.202 \pm 0.374$, according to this all the β^S values shown in the Table below are within 1.3σ CL with respect to $\langle\beta\rangle^S$. For large angles scrutiny the mean for these 10 regions is $\langle\beta\rangle^L = 1.498 \pm 0.271$, according to this all the β^L values are within 1.4σ CL with respect to $\langle\beta\rangle^L$. The comparison of the 2PACF from the 10 regions, displayed in Figure 5.1, suggests further analyses that we perform in the Subsection 5.2.

	θ_0^S [degrees]	β^S	θ_0^L [degrees]	β^L
Area 1	0.299	2.004	0.304	2.059
Area 2	0.181	0.848	0.295	1.209
Area 3	0.259	1.249	0.312	1.649
Area 4	0.256	1.384	0.289	1.634
Area 5	0.197	1.031	0.265	1.349
Area 6	0.235	1.286	0.276	1.551
Area 7	0.252	1.174	0.311	1.601
Area 8	0.263	1.468	0.282	1.609
Area 9	0.258	0.851	0.280	1.063
Area 10	0.201	0.727	0.318	1.253

5.2 Sky patches with intriguing features

According to the literature (KEENAN *et al.*, 2013), the Area 2 partially shares the region of the sky where the projected Local Cosmic Void (LCV) is located. This turns the Area 2 an interesting arena to assess, with diverse statistical methodologies, the possible imprints left by the LCV in our analyses. We also notice that Area 9 and Area 10 show a 2PACF similar to Area 2 (see Figure 5.1), a fact that may indicate that these two regions also have features suggestive of the presence of projected cosmic voids, like Area 2 does.

Let us concentrate first on the study of Area 2, where we observe features that can be a signature of the presence of the projected LCV there.

- First, we notice that the Area 2 overlaps the sky region where diverse astronomical studies have reported or a huge low-density region (KEENAN *et al.*, 2013) or the LCV (TULLY *et al.*, 2019). An *underdense* region, also referred as a *low-density* region, is a spatial region characterized by a density contrast $\delta < 0$, which means less matter content inside that volume with respect to the density measured in a largest volume. Moreover, we also notice that the Areas 9 and 10 are close to the sky location where the Dipole Repeller was detected (HOFFMAN *et al.*, 2017).

- From the 2PACF studies, as shown in the plots of Figure 5.1, one immediately notices that the Area 2 (but not only) exhibits a consistent lack of correlations over a large angle range. This feature indicates, as we shall prove in a separate Subsection,

that this sky region is, indeed, underdense. For this reason, we find interesting to study in more detail the angular correlations in the Area 2 with the PH and LS estimators, with the first one being more intuitive to reveal voids than the second one. Interestingly, this signature is also noticed in the 2PACF of Areas 9 and 10.

- A toy-model simulation, described in detail in the next Subsection, shows that the signature observed in Area 2 (a close inspection shows the same signature also in Areas 9 and 10) is well represented by a void region of $\sim 9^{\circ}$ of radius and with density contrast $\delta \simeq -0.7$, which means 30% less objects content with respect to the density measured in a largest volume (or respect to a density measured far from this region; see, e.g., KEENAN *et al.* (2013)). In other words, underdense regions or voids projected on the sky produce, indeed, the signature observed in the 2PACF shown in Area 2.

- The Cumulative Distribution Function on the Area 2 provides important complementary information regarding the geometry of 3D voids projected on the sky, for this, this analysis will be discussed in a next Subsection.

All these evidences together strongly suggest that Areas 2, 9, and 10 overlap 3D projected regions with prevalence of voids. In fact, while Area 2 is next to the LCV (KEENAN *et al.*, 2013; TULLY *et al.*, 2019), the literature reports that Areas 9 and 10 are close to the underdense region termed the *Dipole Repeller* (HOFFMAN *et al.*, 2017). In the following Subsections we discuss in detail these evidences.

5.2.1 Cumulative Distribution Function

One can investigate whether the feature found in Area 2 corresponds indeed to a projection of a series of small voids along the line-of-sight. For this aim, we also use the distance information available in the ALFALFA catalogue. The distance distribution of the sample corresponding to Area 2 is shown in Figure 5.3[2].

We determine the cumulative distribution function (CDF), which is defined as the probability that a random variable X has a value less than or equal to x in the interval $F_X : \mathbb{R} \rightarrow [0, 1]$ (WASSERMAN, 2004),

$$F_X(x) = \mathbb{P}(\mathrm{X} \leqslant \mathrm{x}). \tag{5.1}$$

The theoretical curve is calculated for a Gaussian distribution with probability density

[2]Note that there is the possibility that the ALFALFA survey may not have detected all the low-luminosity sources present in the Local Universe due to the luminosity threshold of the instrument. However, in this respect, we are considering that the observational scheme of the ALFALFA survey was planned to avoid, or minimize, this possibility.

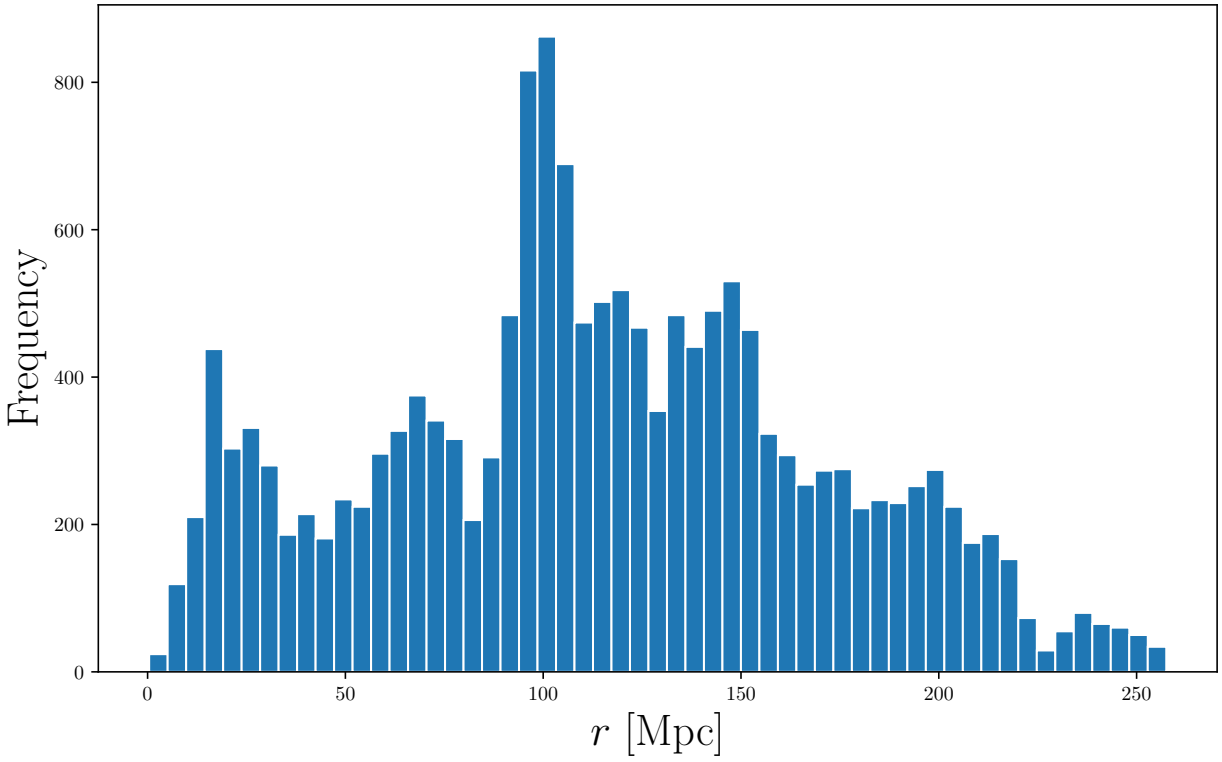

Figure 5.3: Distance distribution histogram of the ALFALFA sample used in the analyses. The distance information is used in the calculation of the Cumulative Distribution Functions (see the Subsection 5.2.1).

function (PDF) defined as

$$P(x) = \frac{1}{\sigma\sqrt{2\pi}} \exp\left[-\frac{1}{2}\left(\frac{x-\mu}{\sigma}\right)^2\right], \tag{5.2}$$

where σ is the standard deviation and μ is the mean of the distribution of the variable x, that, in our case, are the distances of the cosmic objects (BEVINGTON and ROBINSON, 2003).

We plot the theoretical CDF considering the basic features of the data in analysis and compute, and plot together, the CDF for the Area 2 data set (see Figure 5.4). The theoretical CDF was plotted using 44 bins, and has mean $\mu = 116$ Mpc, and standard deviation $\sigma = 56$ Mpc. Examining both CDFs, from data in Area 2 and the theoretical one, shown in Figure 5.4, one clearly observes two depressions suggestive of underdense regions: one not so large around $r \in [100, 140]$ Mpc and the other is larger and deeper at $r \in [160, 245]$ Mpc. Due to the proximity of these depressions, and moreover, from the analyses of really of MOORMAN *et al.* (2014), the voids network may indeed interconnect small and medium size voids that can be interpreted as a very large void. Therefore, we conclude that the void structure projected onto Area 2 has the approximate location $100\,\text{Mpc} \lesssim r \lesssim 240\,\text{Mpc}$, which corresponds to an underdense region of ~ 140 Mpc in length, and width of the order of 60 Mpc.

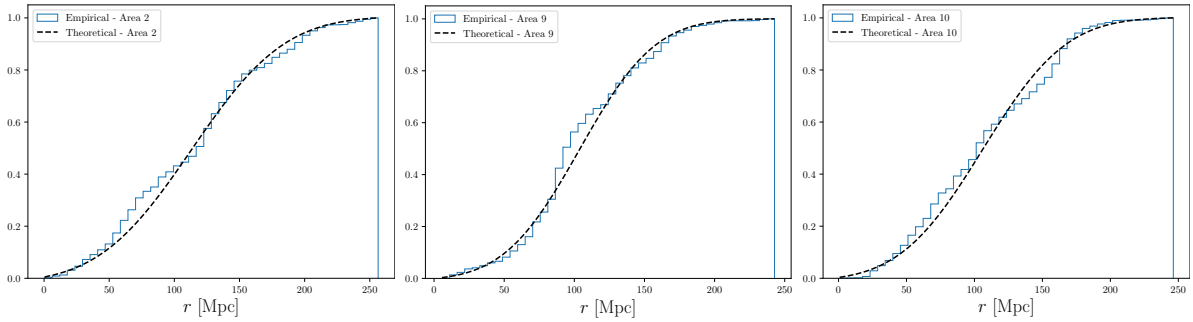

Figure 5.4: Analysis of the Areas 2, 9, and 10 with the Cumulative Distribution Function. **Left Panel, Area 2:** This function shows clearly two depressions suggestive of underdense regions: one not so large around $r \in [100, 140]$ Mpc and the other is larger and deeper at $r \in [160, 240]$ Mpc. Due to the proximity of these depressions, and moreover, as suggested by the analyses of MOORMAN *et al.* (2014), the voids network may interconnect small and medium size voids that can be interpreted as a very large void. Therefore, we conclude that the void structure projected onto Area 2 has an approximate length of $100\,\text{Mpc} \lesssim r \lesssim 240\,\text{Mpc}$, which corresponds to an underdense region with size around 140 Mpc, and width of the order of 60 Mpc. **Midle Panel, Area 9:** Similarly, there is one depression around $r \in [40, 90]$ Mpc, and another around $r \in [140, 190]$ Mpc. **Right Panel, Area 10:** This plot shows one deep depression around $r \in [130, 180]$ Mpc. In all cases the theoretical CDF was plotted using 44 bins, with mean $\mu = 116$ Mpc and standard deviation $\sigma = 56$.

Our results are compatible with the analyses done by MOORMAN *et al.* (2014), who studied the underdensity regions of the ALFALFA data in more detail (c.f. Figure 1 therein). The CDF of Area 2 shows the presence of distance intervals where there are fewer objects than expected when comparing with the Gaussian curve of Equation (5.2) and that, in fact, it would not correspond to a single giant void, but to some contiguous and (probably) connected smaller voids.

5.3 LS versus PH

We have commented above that the PH estimator is more intuitive than the LS estimator in the description of regions with clustered matter and voids. This happens due to the direct comparison between the ratio of data pairs and random pairs with unity, and this feature shall be tested in the following toy-model simulation.

As commented above, the sky region named Area 2 shares in part the region containing the projected LCV (KEENAN *et al.*, 2013), and this fact might be correlated with the signature of a large depression –although not so deep in the LS 2PACF– observed in the plot of the Area 2 in Figure 5.1. Our intention is to investigate whether this feature is a possible signature of the LCV.

Consider a simulated sky region with the same features as the Area 2, that is, same angular scale dimensions and number of cosmic objects therein. Remove 30% of objects

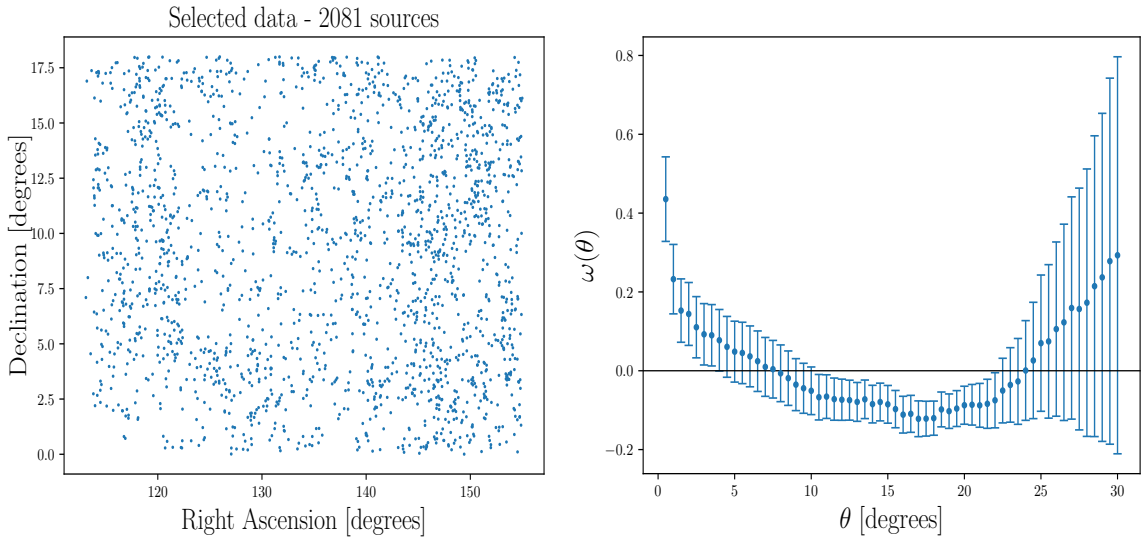

Figure 5.5: **Left panel:** Cartesian projection of the Spring sky region named Area 2, containing 2081 cosmic sources in an area of $\sim$ 756 deg^2. **Right panel:** 2PACF using the PH estimator for the data in Area 2.

located inside a disc of 9° of radius[3] and redistribute these objects uniformly outside the disc. Our results can be observed in Figure 5.6 where we show the original region with uniformly distributed data and the region after one removes 30% of objects from a 9° of radius disc. Now we perform the 2PACF for the simulated void catalog using both estimators, i.e., PH and LS. The curves can be seen in Figure 5.7.

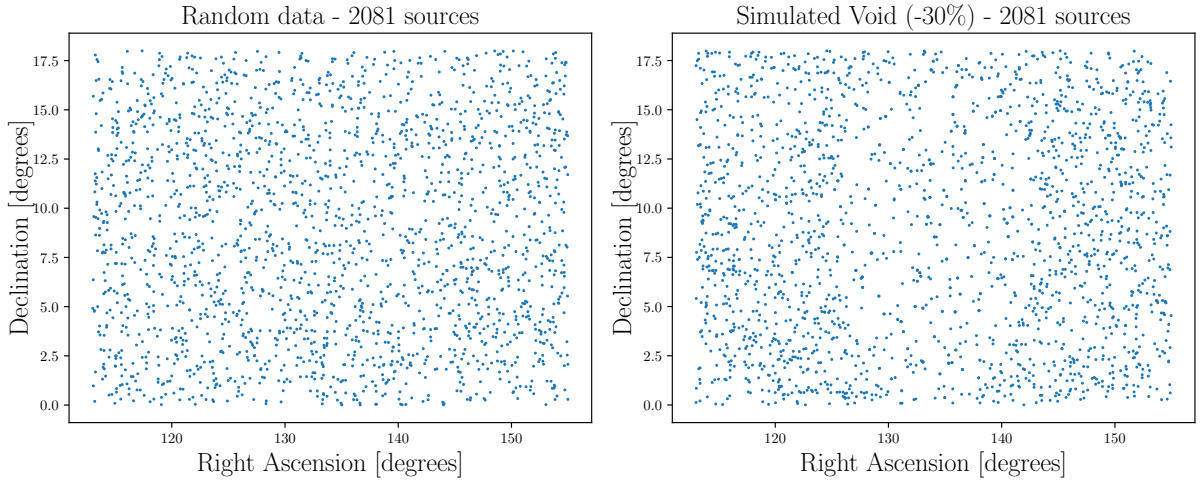

Figure 5.6: Toy-model experiment, simulating a void region with $\delta = -0.7$: Area 2 simulated region with 2081 uniformly distributed objects (left panel), and the same region but with 30% of the cosmic objects removed from a disc of 9° and distributed randomly outside the disc (right panel).

From the results observed in Figure 5.7, we conclude that a void characterized with

[3]The location of the disc centre that simulates the artificial void is not relevant because for the 2PACF what matters is the distance between pairs.

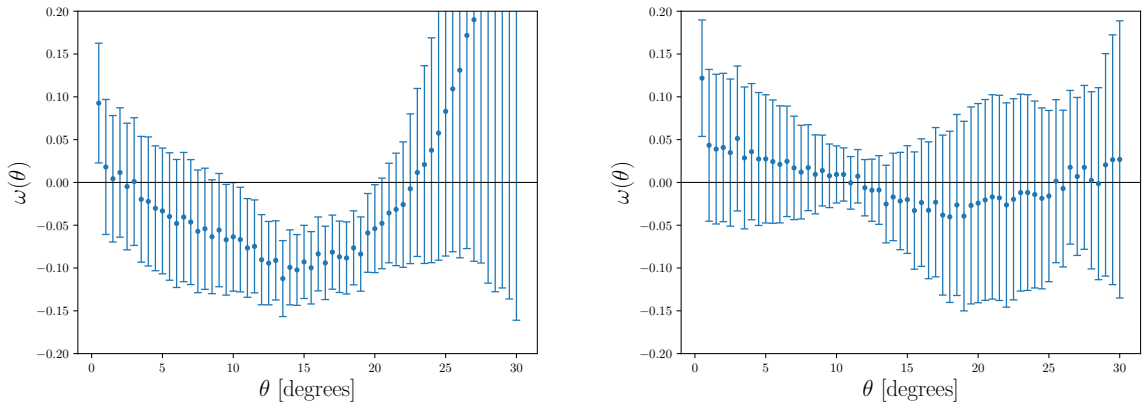

Figure 5.7: 2PACF analyses for a toy-model simulation, where an artificial void, with $\delta = -0.7$ and radius of 9°, was produced to compare the descriptions of it given by the PH (left panel) and the LS (right panel) estimators.

number density contrast $\delta = -0.7$ can be clearly detected with the 2PACF-PH estimator but not with the 2PACF-LS estimator. The large depression signature observed in the 2PACF of Area 2, shown in Figure 5.1, is indeed the signature of a large underdense region, therefore our analyses confirm the presence of (part of) the projected LCV in the Area 2 (KEENAN *et al.*, 2013; TULLY *et al.*, 2019). As this underdense-region signature is also observed in the 2PACF of Areas 9 and 10, we are led to conclude that the 2PACF also manifest a large underdense region projected there, and due to its proximity it is very likely that this void structure is (part of) the projected *Dipole Repeller* (HOFFMAN *et al.*, 2017). Figure 5.8 illustrates the approximate position, but not the true extension, of these underdensity regions.

5.4 Robustness, consistency, and null tests

To probe the statistical isotropy of the Local Universe, and to give support to our findings, we elaborate a series of sensitivity and robustness tests. Some of them were introduced along the text, like the toy-model simulation, for instance. In this Section we test a random catalog to verify that it does not produce any signature in the 2PACF; our result can be observed in Figure 5.9.

Moreover, for small-angle analyses we analyse the best-fit parameter β^S from a set of 1000 Area-mocks, produced under the statistical isotropy hypothesis, to compute the statistical significance of the parameter β^S obtained from the 10 regions in analysis displayed in Table 5.1. The distribution of β^S-values shown in Figure 5.10 shows that $\beta^{S;SI} = 1.180 \pm 0.325$. In consequence, this result lead us to conclude that for small-angle analyses the 10 regions in which we divided the ALFALFA footprint are statistically isotropic within 1.4σ CL.

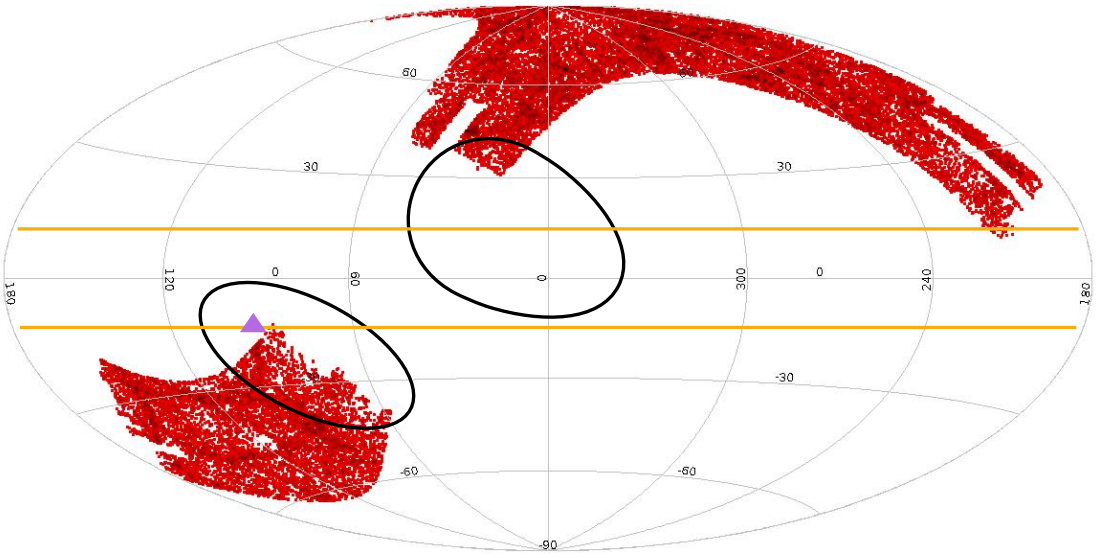

Figure 5.8: The ALFALFA footprint in Galactic coordinates. The enclosed lines show, illustratively, the regions containing the projected underdense regions that could have left imprints in the data sample analysed. The horizontal lines, $\sim 15^{\circ}$ above and below the equator, represent the zone of avoidance, that is, the sky region where visible light is obscured by the Milky Way plane. The center of the picture corresponds to the galactic centre, and above and below the equator one has the NGH and SGH, respectively. The small (violet) triangle denotes the approximate position of the Dipole Repeller (HOFFMAN *et al.*, 2017).

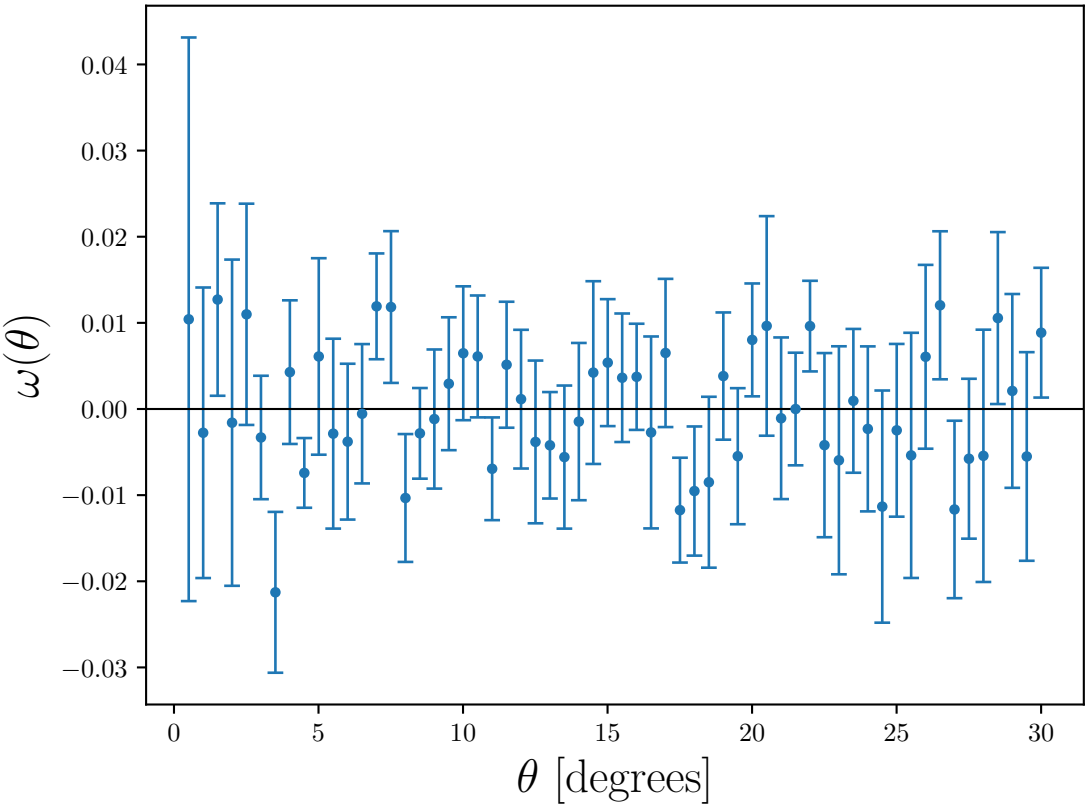

Figure 5.9: Null test for the random dataset. We perform the 2PACF analysis considering one random catalogue as a *pseudo* data catalogue. As observed, the 2PACF evidences no signature, just statistical fluctuations.

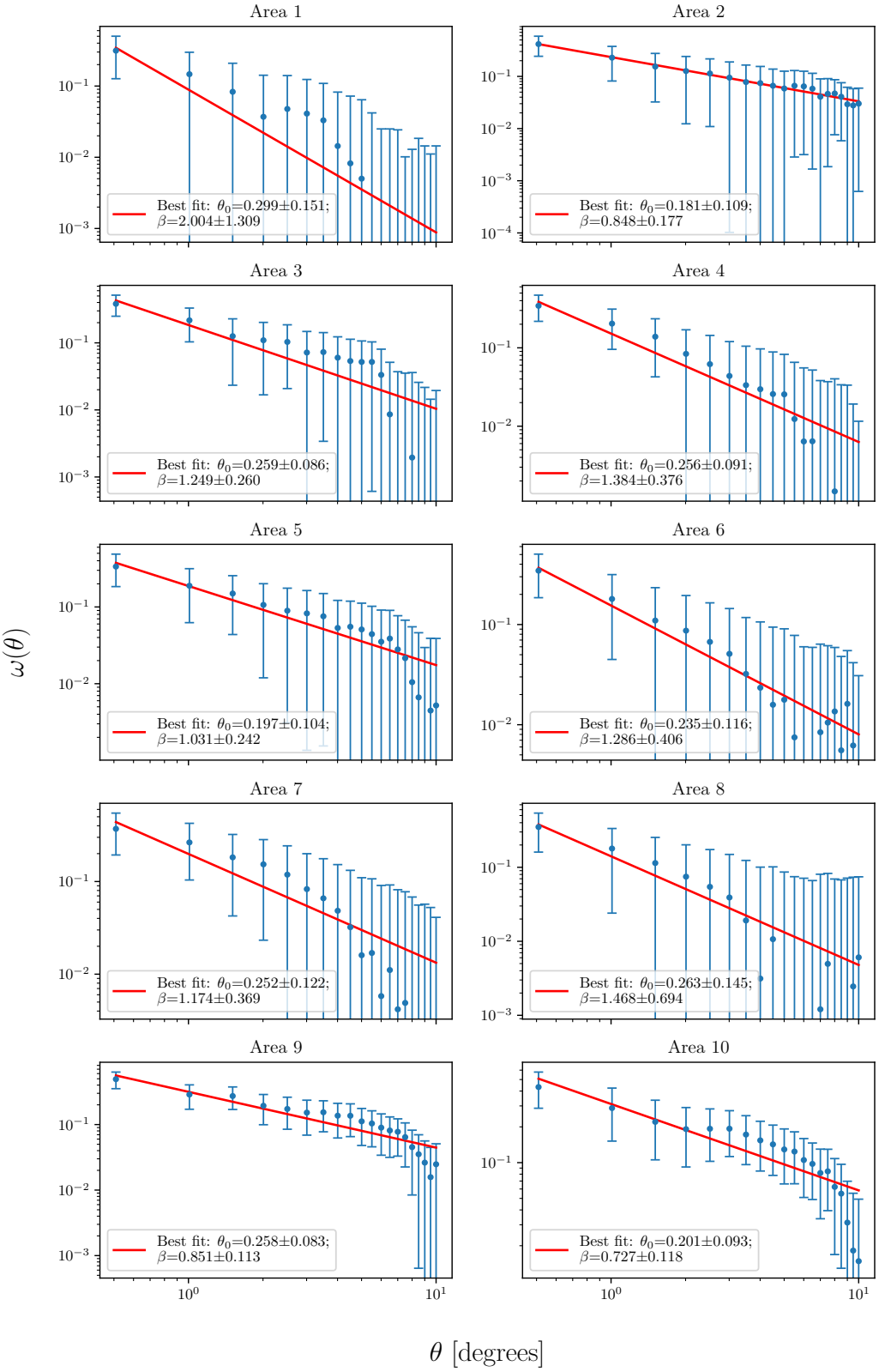

Figure 5.10: Mosaic of the 2PACF for *small-angle analysis*: angular distribution study of the 10 sky patches in which we divided the ALFALFA footprint, using the 2PACF with the LS estimator for the small angular interval, i.e., $0^\circ < \theta < 10^\circ$.

Chapter 6

Conclusions

This dissertation conducted independent model analyses to study the statistical isotropy in the Local Universe (LU) using data from the ALFALFA catalog ($z < 0.06$). Given the significance of the Cosmological Principle (CP) for the concordance model, testing and validating isotropy is of recognized importance in the scientific community.

The application of the CP to the LU is another crucial point, as the LU, despite being close to us, is difficult to observe due to the presence of the Milky Way disc, which hinders the observation of extragalactic objects in the visible range of the electromagnetic spectrum. On the other hand, there is a large area mapped by astronomical surveys, with observed region in opposite Galactic hemispheres that can be investigated.

In this work, we investigated the angular distribution of the HI cosmological tracer, which provided us with information about matter and void structures in the LU. For this purpose, we selected data classified as Code 1 - considered to be $\sim 100\%$ reliable according to the ALFALFA team - and divided our final sample into ten approximately $750\,\mathrm{deg}^2$ areas. This division needed to be done in such a way that each region was not too large –which would reduce the available data for analysis– nor too small with low number density. We adopted the criterion of the homogeneity scale (with a value of $\theta_H \simeq 20^\circ$ when the matter bias is $b \simeq 1$). Furthermore, each patch was carefully delineated to avoid the presence of irregular shapes that could hinder the reproduction of each region as synthetic catalogs.

Our statistical analyses were performed using the Landy-Szalay estimator of the two-point angular correlation function in each of the ten regions. With this, we investigated the behavior of the ALFALFA angular distribution and compared it to what would be expected for a 2PACF obtained under the assumption of homogeneity and isotropy. Our results are summarized in Table 5.1 and Figures 5.1 and 5.10. Thanks to recent efforts dedicated to investigating the structures in the LU, today we have knowledge about the spatial distribution of clustered matter and voids. This valuable information provides a

reasonable explanation for the intriguing behavior observed in the 2PACF.

Our results at small scales (Figure 5.10) served to obtain the fitting parameter β, which is necessary to quantify the level of isotropy in our samples. By comparing the values from the ten regions, we found that the median of the β distribution was $\beta^s = 1.180 \pm 0.325$, leading us to conclude that there is compatibility with statistical isotropy within 1.4σ CL.

However, as we increase the considered scale size, we found intriguing peculiarities in some regions, as illustrated in Figure 5.1. In particular, Areas 2, 9, and 10 exhibit a significant depression indicative of the presence of a large underdensity - or a collection of subdensities - that may have a common origin in a void with a density contrast of $\delta \simeq -0.7$, as discussed in Chapter 5. Areas 9 and 10, for example, are very close to the location of the Dipole Repeller. Focusing on Area 2, we found that it overlaps with the location where several previous studies have reported the presence of a Local Cosmic Void. We also applied the PH estimator to our data to compare the behavior of the obtained curves, because the PH estimator is more intuitive, and it better highlights the presence of underdensities and overdensities, contrary to what occurs with the LS estimator. The presence of an underdensity in this region was tested through a toy-model experiment, which showed that Area 2 is well-sourced by a void region of 9° and with a density contrast of $\delta \simeq -0.7$.

Finally, we complemented our tests using the cumulative distribution function and compared the distance intervals where empirical values remained below the theoretical expectation with the possible positions of voids found by MOORMAN *et al.* (2014). Thus, we conclude that the void structure projected onto Area 2 has the approximate location $100\,\mathrm{Mpc} \lesssim r \lesssim 245\,\mathrm{Mpc}$, which corresponds to an underdense region of ~ 150 Mpc in lenght, and width of the order of 60 Mpc, and agrees well with the literature.

Bibliography

ADLER, R. J., 2010, *The geometry of random fields*. Springer New York, NY, SIAM.

AGRAWAL, A., MAKIYA, R., CHIANG, C.-T., et al., 2017, "Generating log-normal mock catalog of galaxies in redshift space", J. Cosmology Astropart. Phys., 2017(10):003. doi: 10.1088/1475-7516/2017/10/003.

ALURI, P. K., SHAFIELOO, A., 2017, "Power asymmetry in CMB polarization maps from PLANCK : a local variance analysis", *arXiv e-prints*, art. arXiv:1710.00580. doi: 10.48550/arXiv.1710.00580.

ALURI, P. K., RALSTON, J. P., WELTMAN, A., 2017, "Alignments of parity even/odd-only multipoles in CMB", Mon. Not, Roy. Astron. Soc., v. 472, n. 2 (dez.), pp. 2410–2421. doi: 10.1093/mnras/stx2112.

ALURI, P. K., CEA, P., CHINGANGBAM, P., et al., 2022, "Is the Observable Universe Consistent with the Cosmological Principle?" *arXiv e-prints*, art. arXiv:2207.05765.

APPLEBY, S., SHAFIELOO, A., 2014, "Testing isotropy in the local Universe", J. Cosmology Astropart. Phys., v. 2014, n. 10 (out.), pp. 070–070. doi: 10.1088/1475-7516/2014/10/070.

AVILA, F., NOVAES, C. P., BERNUI, A., et al., 2019, "The angular scale of homogeneity in the local Universe with the SDSS blue galaxies", Mon. Not, Roy. Astron. Soc., v. 488, n. 1 (set.), pp. 1481–1487. doi: 10.1093/mnras/stz1765.

AVILA, F., BERNUI, A., DE CARVALHO, E., et al., 2021, "The growth rate of cosmic structures in the local Universe with the ALFALFA survey", Mon. Not, Roy. Astron. Soc., v. 505, n. 3 (ago.), pp. 3404–3413. doi: 10.1093/mnras/stab1488.

AVILA, F., NOVAES, C. P., BERNUI, A., et al., 2018, "The scale of homogeneity in the local Universe with the ALFALFA catalogue", *jcap*, 2018(12):041. doi: 10.1088/1475-7516/2018/12/041.

AVILA, F., BERNUI, A., NUNES, R. C., et al., 2022, "The homogeneity scale and the growth rate of cosmic structures", *mnras*, v. 509, n. 2 (jan.), pp. 2994–3003. doi: 10.1093/mnras/stab3122.

BARROW, J. D., COLES, P., 1990, "The statistics of primordial density fluctuations", Mon. Not, Roy. Astron. Soc., v. 244 (maio), pp. 188–192.

BAUMANN, D., 2022, *Cosmology*. New York, NY, Cambridge University Press.

BENGALY, C. A. P., BERNUI, A., FERREIRA, I. S., et al., 2017, "Probing cosmological isotropy with Planck Sunyaev-Zeldovich galaxy clusters", *mnras*, v. 466, n. 3 (abr.), pp. 2799–2804. doi: 10.1093/mnras/stw3233.

BENGALY, C. A. P., SIEWERT, T. M., SCHWARZ, D. J., et al., 2019, "Testing the standard model of cosmology with the SKA: the cosmic radio dipole", *mnras*, v. 486, n. 1 (jun.), pp. 1350–1357. doi: 10.1093/mnras/stz832.

BENGALY, C. A. P., MAARTENS, R., SANTOS, M. G., 2018, "Probing the Cosmological Principle in the counts of radio galaxies at different frequencies", *jcap*, 2018(4):031. doi: 10.1088/1475-7516/2018/04/031.

BERNARDEAU, F., KOFMAN, L., 1995, "Properties of the Cosmological Density Distribution Function", Astrophys. J., v. 443 (abr.), pp. 479. doi: 10.1086/175542.

BERNUI, A., HIPÓLITO-RICALDI, W. S., 2008, "Can a primordial magnetic field originate large-scale anomalies in WMAP data?" Mon. Not, Roy. Astron. Soc., v. 389, n. 3 (set.), pp. 1453–1460. doi: 10.1111/j.1365-2966.2008.13683.x.

BERNUI, A., VILLELA, T., WUENSCHE, C. A., et al., 2006, "On the cosmic microwave background large-scale angular correlations", Astron. Astrophys., v. 454, n. 2 (ago.), pp. 409–414. doi: 10.1051/0004-6361:20054243.

BERNUI, A., MOTA, B., REBOUÇAS, M. J., et al., 2007, "Mapping the large-scale anisotropy in the WMAP data", Astron. Astrophys., v. 464, n. 2 (mar.), pp. 479–485. doi: 10.1051/0004-6361:20065585.

BERNUI, A., FERREIRA, I. S., WUENSCHE, C. A., 2008, "On the Large-Scale Angular Distribution of Short Gamma-Ray Bursts", *apj*, v. 673, n. 2 (fev.), pp. 968–971. doi: 10.1086/524678.

BERNUI, A., OLIVEIRA, A. F., PEREIRA, T. S., 2014, "North-South non-Gaussian asymmetry in Planck CMB maps", J. Cosmology Astropart. Phys., v. 2014, n. 10 (out.), pp. 041–041. doi: 10.1088/1475-7516/2014/10/041.

BERNUI, A., 2008, "Anomalous CMB north-south asymmetry", *prd*, 78(6):063531. doi: 10.1103/PhysRevD.78.063531.

BERNUI, A., 2009, "Is the cold spot responsible for the CMB North-South asymmetry?" Phys. Rev. D, 80(12):123010. doi: 10.1103/PhysRevD.80.123010.

BERNUI, A., VILLELA, T., FERREIRA, I., 2004, "Analysis of the Angular Distribution of Cosmic Objects", *International Journal of Modern Physics D*, v. 13, n. 7 (jan.), pp. 1189–1195. doi: 10.1142/S0218271804005304.

BEVINGTON, P. R., ROBINSON, D. K., 2003, *Data reduction and error analysis for the physical sciences*. New York, NY, McGraw-Hill.

BÖHRINGER, H., CHON, G., COLLINS, C. A., 2020, "Observational evidence for a local underdensity in the Universe and its effect on the measurement of the Hubble constant", Astron. Astrophys., 633:A19. doi: 10.1051/0004-6361/201936400.

BOLEJKO, K., WYITHE, J. S. B., 2009, "Testing the copernican principle via cosmological observations", *jcap*, 2009(2):020. doi: 10.1088/1475-7516/2009/02/020.

COIL, A. L., 2013, "The Large-Scale Structure of the Universe". In: Oswalt, T. D., Keel, W. C. (Eds.), *Planets, Stars and Stellar Systems. Volume 6: Extragalactic Astronomy and Cosmology*, v. 6, Springer, p. 387, Dordrecht. doi: 10.1007/978-94-007-5609-0_8.

COLEMAN, P. H., PIETRONERO, L., 1992, "The fractal structure of the universe", Phys. Rep., v. 213, n. 6 (maio), pp. 311–389. doi: 10.1016/0370-1573(92)90112-D.

COLES, P., JONES, B., 1991, "A lognormal model for the cosmological mass distribution." Mon. Not, Roy. Astron. Soc., v. 248 (jan.), pp. 1–13. doi: 10.1093/mnras/248.1.1.

COLOMBI, S., 1994, "A "skewed" lognormal approximation to the probability distribution function of the large-scale density field." Astrophys. J., v. 435, n. 2 (nov.), pp. 536–539. doi: 10.1086/174834.

CONNOLLY, A. J., SCRANTON, R., JOHNSTON, D., et al., 2002, "The Angular Correlation Function of Galaxies from Early Sloan Digital Sky Survey Data", Astrophys. J., v. 579, n. 1 (nov.), pp. 42–47. doi: 10.1086/342787.

CRESSWELL, J. G., PERCIVAL, W. J., 2009, "Scale-dependent galaxy bias in the Sloan Digital Sky Survey as a function of luminosity and colour", Mon. Not, Roy. Astron. Soc., v. 392, n. 2 (jan.), pp. 682–690. doi: 10.1111/j.1365-2966.2008.14082.x.

DAVIS, M., PEEBLES, P. J. E., 1983, "A survey of galaxy redshifts. V. The two-point position and velocity correlations." *apj*, v. 267 (abr.), pp. 465–482. doi: 10.1086/160884.

DE CARVALHO, E., BERNUI, A., CARVALHO, G. C., et al., 2018, "Angular Baryon Acoustic Oscillation measure at z=2.225 from the SDSS quasar survey", J. Cosmology Astropart. Phys., 2018(4):064. doi: 10.1088/1475-7516/2018/04/064.

DE CARVALHO, E., BERNUI, A., XAVIER, H. S., et al., 2020, "Baryon acoustic oscillations signature in the three-point angular correlation function from the SDSS-DR12 quasar survey", Mon. Not, Roy. Astron. Soc., v. 492, n. 3 (mar.), pp. 4469–4476. doi: 10.1093/mnras/staa119.

DE CARVALHO, E., BERNUI, A., AVILA, F., et al., 2021, "BAO angular scale at $z_{eff} = 0.11$ with the SDSS blue galaxies", Astron. Astrophys., 649:A20. doi: 10.1051/0004-6361/202039936.

DE CARVALHO, E., 2019, *Oscilações acústicas bariônicas nas distribuições de quasares e galáxias azuis*. Tese de Doutorado, Observatório Nacional, Rio de Janeiro, dez.

DI VALENTINO, E., MENA, O., PAN, S., et al., 2021, "In the realm of the Hubble tension-a review of solutions", *Classical and Quantum Gravity*, 38(15):153001. doi: 10.1088/1361-6382/ac086d.

EINSTEIN, A., 1905, "Über einen die Erzeugung und Verwandlung des Lichtes betreffenden heuristischen Gesichtspunkt", *Annalen der Physik*, v. 322, n. 6 (jan.), pp. 132–148. doi: 10.1002/andp.19053220607.

FIXSEN, D. J., 2009, "The Temperature of the Cosmic Microwave Background", Astrophys. J., v. 707, n. 2 (dez.), pp. 916–920. doi: 10.1088/0004-637X/707/2/916.

FIXSEN, D. J., CHENG, E. S., GALES, J. M., et al., 1996, "The Cosmic Microwave Background Spectrum from the Full COBE FIRAS Data Set", Astrophys. J., v. 473 (dez.), pp. 576. doi: 10.1086/178173.

FRANCO, C., AVILA, F., BERNUI, A., 2023, "Probing cosmic isotropy in the Local Universe", submitted.

FRY, J. N., 1986, "Nonlinear statistics and biasing", Astrophys. J. Lett., v. 308 (set.), pp. L71–L74. doi: 10.1086/184747.

FUJII, H., 2022, "Large-scale Homogeneity in the distribution of Quasars in the Hercules-Corona Borealis Great Wall Region", *Serbian Astronomical Journal*, v. 204 (jun.), pp. 29–38. doi: 10.2298/SAJ2204029F.

GALLONI, G., BARTOLO, N., MATARRESE, S., et al., 2022, "Test of the Statistical Isotropy of the Universe using Gravitational Waves", *arXiv e-prints*, art. arXiv:2202.12858.

GONÇALVES, R. S., CARVALHO, G. C., BENGALY, C. A. P., et al., 2018a, "Measuring the scale of cosmic homogeneity with SDSS-IV DR14 quasars", *mnras*, v. 481, n. 4 (dez.), pp. 5270–5274. doi: 10.1093/mnras/sty2670.

GONÇALVES, R. S., CARVALHO, G. C., BENGALY, C. A. P., J., et al., 2018b, "Cosmic homogeneity: a spectroscopic and model-independent measurement", *mnras*, v. 475, n. 1 (mar.), pp. L20–L24. doi: 10.1093/mnrasl/slx202.

GONÇALVES, R. S., CARVALHO, G. C., ANDRADE, U., et al., 2021, "Measuring the cosmic homogeneity scale with SDSS-IV DR16 quasars", *jcap*, 2021(3):029. doi: 10.1088/1475-7516/2021/03/029.

GUAINAZZI, M., MATT, G., PEROLA, G. C., 2005, "X-ray obscuration and obscured AGN in the local universe", *aap*, v. 444, n. 1 (dez.), pp. 119–132. doi: 10.1051/0004-6361:20053643.

HAMILTON, A. J. S., 1993, "Toward Better Ways to Measure the Galaxy Correlation Function", *apj*, v. 417 (nov.), pp. 19. doi: 10.1086/173288.

HANSEN, F. K., BANDAY, A. J., GÓRSKI, K. M., 2004, "Testing the cosmological principle of isotropy: local power-spectrum estimates of the WMAP data", *mnras*, v. 354, n. 3 (nov.), pp. 641–665. doi: 10.1111/j.1365-2966.2004.08229.x.

HAYNES, M. P., GIOVANELLI, R., KENT, B. R., et al., 2018, "The Arecibo Legacy Fast ALFA Survey: The ALFALFA Extragalactic H I Source Catalog", Astrophys. J., 861(1):49. doi: 10.3847/1538-4357/aac956.

HEWETT, P. C., 1982, "The estimation of galaxy angular correlation functions", *mnras*, v. 201 (dez.), pp. 867–883. doi: 10.1093/mnras/201.4.867.

HINSHAW, G., LARSON, D., KOMATSU, E., et al., 2013, "Nine-year Wilkinson Microwave Anisotropy Probe (WMAP) Observations: Cosmological Parameter Results", Astrophys. J. Suppl., 208(2):19. doi: 10.1088/0067-0049/208/2/19.

HOFFMAN, Y., POMARÈDE, D., TULLY, R. B., et al., 2017, "The dipole repeller", *Nature Astronomy*, 1:0036. doi: 10.1038/s41550-016-0036.

HOGG, D. W., EISENSTEIN, D. J., BLANTON, M. R., et al., 2005, "Cosmic Homogeneity Demonstrated with Luminous Red Galaxies", Astrophys. J., v. 624, n. 1 (maio), pp. 54–58. doi: 10.1086/429084.

HUBBLE, E., 1929, "A Relation between Distance and Radial Velocity among Extra-Galactic Nebulae", *Proceedings of the National Academy of Science*, v. 15, n. 3 (mar.), pp. 168–173. doi: 10.1073/pnas.15.3.168.

HUBBLE, E., HUMASON, M. L., 1931, "The Velocity-Distance Relation among Extra-Galactic Nebulae", Astrophys. J., v. 74 (jul.), pp. 43. doi: 10.1086/143323.

HWANG, H. S., GELLER, M. J., 2013, "Dust-obscured Galaxies in the Local Universe", *apj*, 769(2):116. doi: 10.1088/0004-637X/769/2/116.

JONES, M. G., PAPASTERGIS, E., HAYNES, M. P., et al., 2016, "Environmental dependence of the H I mass function in the ALFALFA 70% catalogue", Mon. Not, Roy. Astron. Soc., v. 457, n. 4 (abr.), pp. 4393–4405. doi: 10.1093/mnras/stw263.

KEENAN, R. C., BARGER, A. J., COWIE, L. L., 2013, "Evidence for a ~300 Megaparsec Scale Under-density in the Local Galaxy Distribution", Astrophys. J., 775(1):62. doi: 10.1088/0004-637X/775/1/62.

KEIHÄNEN, E., KURKI-SUONIO, H., LINDHOLM, V., et al., 2019, "Estimating the galaxy two-point correlation function using a split random catalog", Astron. Astrophys., 631:A73. doi: 10.1051/0004-6361/201935828.

KERSCHER, M., SZAPUDI, I., SZALAY, A. S., 2000, "A Comparison of Estimators for the Two-Point Correlation Function", Astrophys. J. Lett., v. 535, n. 1 (maio), pp. L13–L16. doi: 10.1086/312702.

KHAN, M. I., SAHA, R., 2022, "Isotropy statistics of CMB hot and cold spots", *jcap*, 2022(6):006. doi: 10.1088/1475-7516/2022/06/006.

KIRSHNER, R. P., 2004, "Hubble's diagram and cosmic expansion", *Proceedings of the National Academy of Science*, v. 101, n. 1 (jan.), pp. 8–13. doi: 10.1073/pnas.2536799100.

KOFMAN, L., BERTSCHINGER, E., GELB, J. M., et al., 1994, "Evolution of One-Point Distributions from Gaussian Initial Fluctuations", Astrophys. J., v. 420 (jan.), pp. 44. doi: 10.1086/173541.

KURKI-SUONIO, H., 2023. "Galaxy Survey Cosmology". Feb. Disponível em: <https://www.mv.helsinki.fi/home/hkurkisu/GSC1.pdf>.

LANDY, S. D., SZALAY, A. S., 1993, "Bias and Variance of Angular Correlation Functions", *apj*, v. 412 (jul.), pp. 64. doi: 10.1086/172900.

LAURENT, P., LE GOFF, J.-M., BURTIN, E., et al., 2016, "A 14 h^{-3} Gpc^3 study of cosmic homogeneity using BOSS DR12 quasar sample", J. Cosmology Astropart. Phys., 2016(11):060. doi: 10.1088/1475-7516/2016/11/060.

LEMAÎTRE, G., 1927, "Un Univers homogène de masse constante et de rayon croissant rendant compte de la vitesse radiale des nébuleuses extra-galactiques", *Annales de la Société Scientifique de Bruxelles*, v. 47 (jan.), pp. 49–59.

LIDDLE, A., 2003, *An Introduction to Modern Cosmology, Second Edition*. West Sussex, John Wiley & Sons Ltd.

LIMA NETO, G. B., 2022. "Astronomia Extragaláctica". Feb. Disponível em: <http://www.astro.iag.usp.br/~gastao/Extragal.html>.

MARQUES, G. A., NOVAES, C. P., BERNUI, A., et al., 2018, "Isotropy analyses of the Planck convergence map", *mnras*, v. 473, n. 1 (jan.), pp. 165–172. doi: 10.1093/mnras/stx2240.

MARQUES, G. A., BERNUI, A., 2020, "Tomographic analyses of the CMB lensing and galaxy clustering to probe the linear structure growth", J. Cosmology Astropart. Phys., 05(5):052. doi: 10.1088/1475-7516/2020/05/052.

MARTIN, A. M., GIOVANELLI, R., HAYNES, M. P., et al., 2012, "The Clustering Characteristics of H I-selected Galaxies from the 40% ALFALFA Survey", Astrophys. J., 750(1):38. doi: 10.1088/0004-637X/750/1/38.

MATHER, J. C., CHENG, E. S., EPLEE, R. E., J., et al., 1990, "A Preliminary Measurement of the Cosmic Microwave Background Spectrum by the Cosmic Background Explorer (COBE) Satellite", Astrophys. J. Lett., v. 354 (maio), pp. L37. doi: 10.1086/185717.

MOORMAN, C. M., VOGELEY, M. S., HOYLE, F., et al., 2014, "The H I mass function and velocity width function of void galaxies in the Arecibo Legacy Fast ALFA Survey", Mon. Not, Roy. Astron. Soc., v. 444, n. 4 (nov.), pp. 3559–3570. doi: 10.1093/mnras/stu1674.

MYERS, A. D., OUTRAM, P. J., SHANKS, T., et al., 2005, "On statistical lensing and the anticorrelation between 2dF QSOs and foreground galaxies", Mon. Not, Roy. Astron. Soc., v. 359, n. 2 (maio), pp. 741–754. doi: 10.1111/j.1365-2966.2005.08955.x.

NADATHUR, S., 2013, "Seeing patterns in noise: gigaparsec-scale 'structures' that do not violate homogeneity", Mon. Not, Roy. Astron. Soc., v. 434, n. 1 (set.), pp. 398–406. doi: 10.1093/mnras/stt1028.

NORBERG, P., BAUGH, C. M., GAZTAÑAGA, E., et al., 2009, "Statistical analysis of galaxy surveys - I. Robust error estimation for two-point clustering statistics", Mon. Not, Roy. Astron. Soc., v. 396, n. 1 (jun.), pp. 19–38. doi: 10.1111/j.1365-2966.2009.14389.x.

PADMANABHAN, T., 1993, *Structure Formation in the Universe*. New York, NY, Press Syndicate of the University of Cambridge.

PANDEY, B., KULKARNI, G., BHARADWAJ, S., et al., 2011, "The size of the longest filament in the luminous red galaxy distribution", Mon. Not, Roy. Astron. Soc., v. 411, n. 1 (fev.), pp. 332–336. doi: 10.1111/j.1365-2966.2010.17686.x.

PAPASTERGIS, E. M., 2013, *Statistical analysis of ALFALFA galaxies: Insights in galaxy formation & near-field cosmology*. Tese de Doutorado, Cornell University, New York, jan.

PEEBLES, P. J. E., 2001, "The Void Phenomenon", Astrophys. J., v. 557, n. 2 (ago.), pp. 495–504. doi: 10.1086/322254.

PEEBLES, P. J. E., 1981, *The Large-Scale Structure of the Universe*. Princeton, New Jersey, Princeton University Press.

PEEBLES, P. J. E., 1993, *Principles of Physical Cosmology*. Princeton, N.J, Princeton University Press. doi: 10.1515/9780691206721.

PEEBLES, P. J. E., HAUSER, M. G., 1974, "Statistical Analysis of Catalogs of Extragalactic Objects. III. The Shane-Wirtanen and Zwicky Catalogs", *apjs*, v. 28 (nov.), pp. 19. doi: 10.1086/190308.

PEEBLES, P. J. E., NUSSER, A., 2010, "Nearby galaxies as pointers to a better theory of cosmic evolution", Nature, v. 465, n. 7298 (jun.), pp. 565–569. doi: 10.1038/nature09101.

PERLMUTTER, S., ALDERING, G., GOLDHABER, G., et al., 1999, "Measurements of Ω and Λ from 42 High-Redshift Supernovae", Astrophys. J., v. 517, n. 2 (jun.), pp. 565–586. doi: 10.1086/307221.

PETTINI, M., 2018. "Introduction to Cosmology". Disponível em: <https://people.ast.cam.ac.uk/~pettini/IntroCosmology/>.

PLANCK COLLABORATION, AGHANIM, N., AKRAMI, Y., et al., 2020a, "Planck 2018 results. VI. Cosmological parameters", Astron. Astrophys., 641:A6. doi: 10.1051/0004-6361/201833910.

PLANCK COLLABORATION, AKRAMI, Y., ASHDOWN, M., et al., 2020b, "Planck 2018 results. VII. Isotropy and statistics of the CMB", Astron. Astrophys., 641: A7. doi: 10.1051/0004-6361/201935201.

PLIONIS, M., BASILAKOS, S., 2002, "The size and shape of local voids", Mon. Not, Roy. Astron. Soc., v. 330, n. 2 (fev.), pp. 399–404. doi: 10.1046/j.1365-8711. 2002.05069.x.

POLASTRI, L., GRUPPUSO, A., NATOLI, P., 2015, "CMB low multipole alignments in the ΛCDM and dipolar models", J. Cosmology Astropart. Phys., v. 2015, n. 4 (abr.), pp. 018–018. doi: 10.1088/1475-7516/2015/04/018.

RASSAT, A., STARCK, J. L., PAYKARI, P., et al., 2014, "Planck CMB anomalies: astrophysical and cosmological secondary effects and the curse of masking", J. Cosmology Astropart. Phys., v. 2014, n. 8 (ago.), pp. 006–006. doi: 10.1088/ 1475-7516/2014/08/006.

RIESS, A. G., FILIPPENKO, A. V., CHALLIS, P., et al., 1998, "Observational Evidence from Supernovae for an Accelerating Universe and a Cosmological Constant", Astron. J., v. 116, n. 3 (set.), pp. 1009–1038. doi: 10.1086/300499.

RIESS, A. G., MACRI, L. M., HOFFMANN, S. L., et al., 2016, "A 2.4% Determination of the Local Value of the Hubble Constant", Astrophys. J., 826(1):56. doi: 10.3847/0004-637X/826/1/56.

ROOS, M., 2015, *Introduction to Cosmology, Third Edition.* West Sussex, John Wiley & Sons Ltd.

RUBIN, V. C., FORD, W. K., J., THONNARD, N., 1980, "Rotational properties of 21 SC galaxies with a large range of luminosities and radii, from NGC 4605 (R=4kpc) to UGC 2885 (R=122kpc)." Astrophys. J., v. 238 (jun.), pp. 471– 487. doi: 10.1086/158003.

RUBIN, V. C., BURSTEIN, D., FORD, W. K., J., et al., 1985, "Rotation velocities of 16 SA galaxies and a comparison of Sa, SB and SC rotation properties." Astrophys. J., v. 289 (fev.), pp. 81–104. doi: 10.1086/162866.

RYDEN, B., 2003, *Introduction to cosmology.* New York, NY, Cambridge University Press.

SARKAR, P., YADAV, J., PANDEY, B., et al., 2009, "The scale of homogeneity of the galaxy distribution in SDSS DR6", Mon. Not, Roy. Astron. Soc., v. 399, n. 1 (out.), pp. L128–L131. doi: 10.1111/j.1745-3933.2009.00738.x.

SARKAR, P., PANDEY, B., SARKAR, S., 2022, "The maximum extent of the filaments and sheets in the cosmic web: an analysis of the SDSS DR17", *arXiv e-prints*, art. arXiv:2208.09472.

SARKAR, S., PANDEY, B., 2016, "An information theory based search for homogeneity on the largest accessible scale", Mon. Not, Roy. Astron. Soc., v. 463, n. 1 (nov.), pp. L12–L16. doi: 10.1093/mnrasl/slw145.

SCHUTZ, B., 2009, *A First Course in General Relativity*. New York, NY, Cambridge University Press.

SCRIMGEOUR, M. I., DAVIS, T., BLAKE, C., et al., 2012, "The WiggleZ Dark Energy Survey: the transition to large-scale cosmic homogeneity", Mon. Not, Roy. Astron. Soc., v. 425, n. 1 (set.), pp. 116–134. doi: 10.1111/j.1365-2966.2012.21402.x.

SECREST, N. J., VON HAUSEGGER, S., RAMEEZ, M., et al., 2021, "A Test of the Cosmological Principle with Quasars", *apjl*, 908(2):L51. doi: 10.3847/2041-8213/abdd40.

SHIN, J., KIM, J., PICHON, C., et al., 2017, "New Fitting Formula for Cosmic Nonlinear Density Distribution", Astrophys. J., 843(1):73. doi: 10.3847/1538-4357/aa74b9.

SPRINGEL, V., FRENK, C. S., WHITE, S. D. M., 2006, "The large-scale structure of the Universe", Nature, v. 440, n. 7088 (abr.), pp. 1137–1144. doi: 10.1038/nature04805.

SYLOS LABINI, F., BARYSHEV, Y. V., 2010, "Testing the Copernican and Cosmological Principles in the local universe with galaxy surveys", *jcap*, 2010(6):021. doi: 10.1088/1475-7516/2010/06/021.

THEUNS, T., 2021. "Physical Cosmology". Disponível em: <http://icc.dur.ac.uk/~tt/Lectures/UA/L4/cosmology.pdf>.

TOTSUJI, H., KIHARA, T., 1969, "The Correlation Function for the Distribution of Galaxies", Publ. Astron. Soc. Japan, v. 21 (jan.), pp. 221.

TULLY, R. B., FISHER, J. R., 1987, *Nearby galaxies Atlas*. New York, NY, Cambridge University Press.

TULLY, R. B., SHAYA, E. J., KARACHENTSEV, I. D., et al., 2008, "Our Peculiar Motion Away from the Local Void", Astrophys. J., v. 676, n. 1 (mar.), pp. 184–205. doi: 10.1086/527428.

TULLY, R. B., COURTOIS, H. M., DOLPHIN, A. E., et al., 2013, "Cosmicflows-2: The Data", *aj*, 146(4):86. doi: 10.1088/0004-6256/146/4/86.

TULLY, R. B., POMARÈDE, D., GRAZIANI, R., et al., 2019, "Cosmicflows-3: Cosmography of the Local Void", Astrophys. J., 880(1):24. doi: 10.3847/1538-4357/ab2597.

UHLEMANN, C., CODIS, S., PICHON, C., et al., 2016, "Back in the saddle: large-deviation statistics of the cosmic log-density field", Mon. Not, Roy. Astron. Soc., v. 460, n. 2 (ago.), pp. 1529–1541. doi: 10.1093/mnras/stw1074.

VARGAS-MAGAÑA, M., BAUTISTA, J. E., HAMILTON, J. C., et al., 2013, "An optimized correlation function estimator for galaxy surveys", Astron. Astrophys., 554:A131. doi: 10.1051/0004-6361/201220790.

VOGELSBERGER, M., GENEL, S., SPRINGEL, V., et al., 2014, "Introducing the Illustris Project: simulating the coevolution of dark and visible matter in the Universe", Mon. Not, Roy. Astron. Soc., v. 444, n. 2 (out.), pp. 1518–1547. doi: 10.1093/mnras/stu1536.

WANG, Y., BRUNNER, R. J., DOLENCE, J. C., 2013, "The SDSS galaxy angular two-point correlation function", Mon. Not, Roy. Astron. Soc., v. 432, n. 3 (jul.), pp. 1961–1979. doi: 10.1093/mnras/stt450.

WASSERMAN, L., 2004, *Random Variables*. New York, NY, Springer New York. ISBN: 978-0-387-21736-9. doi: 10.1007/978-0-387-21736-9_2. Disponível em: <https://doi.org/10.1007/978-0-387-21736-9_2>.

WHITBOURN, J. R., SHANKS, T., 2014, "The local hole revealed by galaxy counts and redshifts", *mnras*, v. 437, n. 3 (jan.), pp. 2146–2162. doi: 10.1093/mnras/stt2024.

WHITBOURN, J. R., SHANKS, T., 2016, "The galaxy luminosity function and the Local Hole", Mon. Not, Roy. Astron. Soc., v. 459, n. 1 (jun.), pp. 496–507. doi: 10.1093/mnras/stw555.

ZWICKY, F., 1933, "Die Rotverschiebung von extragalaktischen Nebeln", *Helvetica Physica Acta*, v. 6 (jan.), pp. 110–127.

Appendix A

Toy-model simulation of the cumulative distribution function

In order to verify the validity of the results shown in Figure 5.4, a similar robustness test to the simulated void described in Section 5.3 was performed. Utilizing the distance data provided by ALFALFA, we removed a percentage of the data (30%) from intervals of 51 Mpc and generated the same amount with new randomly determined values that are not within the removed interval. Based on this procedure, we arrived at the results presented in Figure A.1.

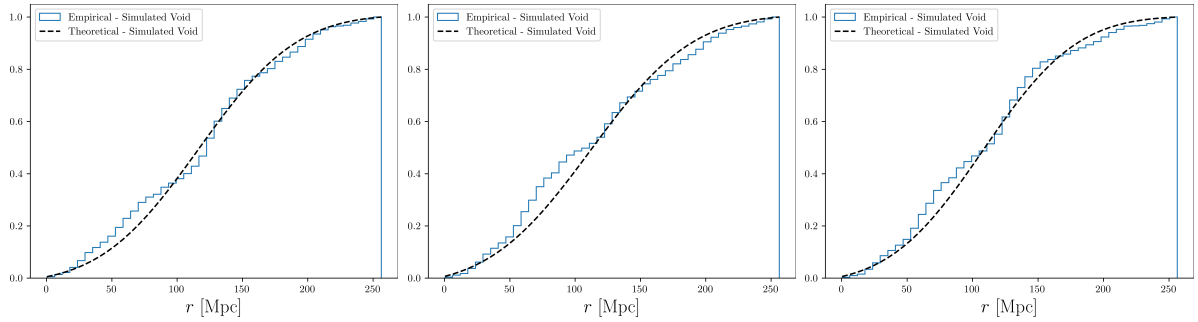

Figure A.1: Toy-model experiment, simulating a void region in three scenarios: (i) data removal in the interval $51 - 102$ Mpc; (ii) data removal in the interval $102 - 153$ Mpc; (iii) data removal in the interval $153 - 204$ Mpc